



1 **Particle size distributions in Earth Sciences: a review of techniques**
2 **and**

3 **a new procedure to match 2D and 3D analyses**

4 Mattia Pizzati^{1*}, Luciana Mantovani¹, Antonio Lisotti², Fabrizio Storti¹ and Fabrizio
5 Balsamo¹

6 ¹University of Parma, Department of Chemistry, Life Sciences, and Environmental Sustainability, 43124
7 Parma, Italy.

8 ²University of Parma, Information Management Area, 43124 Parma, Italy.

9 * Corresponding author, E-mail address: mattia.pizzati@unipr.it, phone number: +39 0521905202

10 **ABSTRACT**

11 Particle size is an essential tool in many research areas including Earth Sciences, Engineering,
12 Material Sciences, Soil Sciences and Pharmacology, among others. Over the last decades,
13 several techniques and methodologies have been developed to calculate particle size
14 distributions on different sample types (i.e., cohesive versus loose), from volumetric (3D) to
15 image-aided (2D) analyses. Here, we (1) present a critical review of most commonly used
16 techniques to calculate particle size distributions from cohesive and loose samples, and (2) we
17 illustrate a new calculation formula to extract reliable 3D grain size distributions from 2D
18 datasets. We propose the use of the "corrected volume-weighted mean diameter" (D_w), as a
19 new particle size descriptor, which results from the summation of products between equivalent
20 particle diameter and particle volume, divided by the total volume of analyzed particles. In this
21 calculation, particles were approximated to perfect circles-spheres, but a shape correction
22 factor was applied to consider deviations from the perfect spherical shape. We tested the
23 accuracy of D_w calculation formula by analyzing 2D datasets acquired from thin sections of 5
24 selected granular sand samples having different mean grain diameters and grain size

Deleted: spanning from

Deleted: spanning



27 distributions (i.e., different sorting degree, grain size distribution width and skewness). Grains
28 were manually digitized, and per each thin section more than 5,000 particles were acquired.
29 Two-dimensional grain size distributions were cross-checked with the results provided via laser
30 diffraction granulometry on the same samples and were compared with previously published
31 and widely used calculation methods. Our promising results encourage the usage of D_w
32 formula as it provides best matching results with 3D laser granulometry and needs basic input
33 parameters that can be easily extracted from any image analysis software.

34

35 **Keywords**

36 Particle size distribution; equivalent diameter; volume-weighted mean diameter; granular
37 materials; image analysis technique; laser diffraction granulometry.

38

39 **1. Introduction**

40 **1.1 Particle size analysis in Earth Sciences and beyond**

41 The quantification of particle size distribution is a fundamental parameter to be determined in
42 different scientific disciplines including Earth and Planetary Sciences, Engineering, Life
43 Sciences, Material Sciences, Soil Sciences, and Pharmacology. Particle size is defined as a
44 scalar property of granular media and is typically calculated as the nominal diameter of
45 particles (Udden, 1914; Wentworth, 1922; Krumbein and Pettijohn, 1938; Krumbein and Sloss,
46 1963; Pettijohn et al., 1972). Particle size is a fundamental component of the texture of granular
47 materials (sediments, rocks, and aggregates) together with particle shape (Wadell, 1935;
48 Krumbein, 1941a; Moss, 1962; Krumbein and Sloss, 1963; Barrett, 1980;

Deleted: spanning from



50 Mora and Kwan, 2000), rounding degree (Wadell, 1933; Powers, 1953; Taylor, 2002), surface
51 morphological features (Wentworth, 1919; Bowman et al., 2001; Russ, 1990), overall fabric
52 (particle preferred orientation) (Griffiths, 1961), and mineralogical composition
53 (Krumbein and Sloss, 1963; Folk, 1974; Boggs, 2009). In particular, in the field of Earth
54 Sciences, particle size determination plays a major role in stratigraphic and sedimentological
55 studies where it provides fundamental information related to the physical and dynamic
56 transport processes (Krumbein, 1941b; Spencer, 1952; Folk and Ward, 1957; Bull, 1962; Sahu,
57 1964; Middleton, 1976; Goldbery and Richardson, 1989; Kranck, 1984; Pickering and Hiscott,
58 2015), provenance and maturity of clastic sediments and rocks (Dapples et al., 1953; Cadigan,
59 1961; Folk, 1974; Boggs, 2009; Garzanti, 2019), fluid storage potential of sedimentary
60 sequences (Fraser, 1935; Griffiths, 1952) and recognition of sedimentary environments (Keller,
61 1945; Buller and McManus, 1973; Mutti, 1992; Selley, 2001; Nichols, 2009). Particle size
62 quantification is also fundamental in structural geology studies, where the correct definition of
63 clast-grain size provides important information to constrain brittle deformation mechanisms
64 from fault rock analysis (Blenkinsop, 1991; Storti et al., 2003; Billi,
65 2005; Heilbronner and Keulen, 2006; Keulen et al., 2007; Luther et al., 2013; Montheil et al.,
66 2020), to understand the overall faulting processes (Engelder, 1974; Sibson, 1977; Marone
67 and Scholz, 1989; Doan and Gary, 2009; Sammis and Ben-Zion, 2008; Balsamo and Storti,
68 2011), and to define plastic deformation styles (Ranalli, 1984; Freeman and Ferguson, 1986;
69 Stipp and Tullis, 2003; Passchier and Trouw, 2005; Hirsch, 2008; Lopez-Sanchez and Llana-
70 Fúnez, 2016). Planetary geology employs the analysis of particle size to unravel sedimentary
71 and surficial transport processes on terrestrial planets of the Solar System (De Pater and
72 Lissauer, 2001; Faure and Mensing, 2007; Bridges and Muhs, 2012; Grotzinger and Milliken,
73 2012), and to study meteoritic bodies (Dodd, 1976; Hughes, 1978a; Martin and Mills, 1978;
74 Eisenhour, 1996). Petrophysics takes into account the evaluation of particle size to understand
75 the primary and secondary porosity and overall fluid flow patterns and magnitude through



76 porous media (Tiab and Donaldson, 2004; Torabi and Fossen, 2009; Balsamo et al., 2010).
77 Hydrogeology studies deal with the quantification of grain size to document fluid pathways in
78 deformed and undeformed rocks and soils (Davis and DeWiest, 1966; Fetter, 1994; Bense et
79 al., 2013). Particle size determination is also important in the field of diagenesis, as in the case
80 of ore-mineral deposits in conjunction with studies regarding structural geology (Jébrak, 1997)
81 or selective cementation of sedimentary sequences (McBride et al., 1995; Mozley and Davis,
82 1996; Morad et al., 2000; Dutton et al., 2002; Cavazza et al., 2009; Van Den Bril and Swennen,
83 2009; Balsamo et al., 2012; Pizzati et al., 2018; Dimmen et al., 2020). Geomorphology employs
84 particle size analysis to identify the products of various geomorphic agents in different
85 environments (marine, fluvial and continental) (Easterbrook, 1969). Glaciology extensively
86 implements particle size determination to quantitatively describe the past and present glacial-
87 related deposits (different types of moraines, tills, and cryo-clastic materials) and to define
88 glacier evolution over time (Washburn, 1979; Molnia, 1983; Eicken, 1993; Menzies, 2000).
89 Particle-crystal size is adopted also in petrology of both intrusive and effusive igneous rocks,
90 where it can provide constraints regarding crystal growth processes occurring inside magma
91 chambers
92 (Higgins, 1994; Means and Park, 1994; Bryon et al., 1995; Higgins, 2000; Zieg and Marsh,
93 2002; Mock and Jerram, 2005; Gualda, 2006; Morgan and Jerram, 2006; Jerram and Higgins,
94 2007; Jerram et al., 2009). Volcanology is particularly interested in particle size analysis to
95 define the magnitude of past eruptions (Kaminski and Jaupart, 1998), to infer the explosivity
96 index (Giachetti et al., 2021) and to characterize the texture and sedimentary transport
97 mechanisms of volcanoclastic deposits (McPhie et al., 1993; Eychenne and Engwell, 2022).
98 The broad list of fields of application reported above helps to understand the critical importance
99 of particle size determination as an effective tool to constrain a wide variety of physical
100 processes. The techniques employed to calculate particle size distribution span from three-
101 dimensional volumetric analysis performed on bulk materials (e.g., classical sieve analysis



102 applied to loose samples) (Udden, 1914) up to two-dimensional automated-manual image
103 analysis (e.g., using thin section images of cohesive samples) (Heilbronner and Barrett, 2014).
104 Nowadays, laser diffraction-based techniques provide accurate, precise, and relatively fast 3D
105 particle size determination and are particularly effective in the case of loose powder samples
106 (Agrawal et al., 1991). In the field of Earth Sciences, rock samples may show different degrees
107 of cohesion, thus implying the use of different techniques in defining grain size distributions.
108 Unfortunately, the direct comparison among results from different analytical procedures is not
109 straightforward, thus limiting the ability of researchers to compare data obtained in different
110 times and from different case studies. This limitation is even more important when results from
111 3D and 2D analyses need to be compared. The reasons for such discrepancy between 3D and
112 2D analyses lie in the type of samples (Cortinovis et al., 2019), number of analyzed particles
113 (Lopez-Sanchez, 2020), particle shape and density (Matthews, 1991a), and instrumental
114 limitations associated with the resolution in the upper and lower grain size ranges (Syvitski et
115 al., 1991a).

Deleted: bi

Deleted: is

Deleted: s

116 In the present contribution, we first provide a critical review of available 3D and 2D analytical
117 techniques employed for grain size calculation and related correction methods. Techniques are
118 critically evaluated highlighting pros, cons, weaknesses, strengths, and applicability on
119 different sample types. Then we focus on defining and testing a new conversion equation to
120 extract 3D average grain diameters from 2D granulometric distributions. To this end, we
121 calculated 2D grain size distributions of 5 selected sand samples through image analysis from
122 petrographic thin sections. The obtained results were corrected with literature methods and
123 with our new equation and were compared with data gained by 3D laser diffraction
124 granulometry technique, which served as reference benchmark. A shape correction factor was
125 applied to the calculated mean diameter to consider particle deviations from the perfect circular
126 shape. In our case, the correction factor was grounded to particle shape, and it slightly varied
127 according to the sample to be analyzed. The volume-weighted mean diameter (D_w) equation

Deleted: revised

Deleted: technique



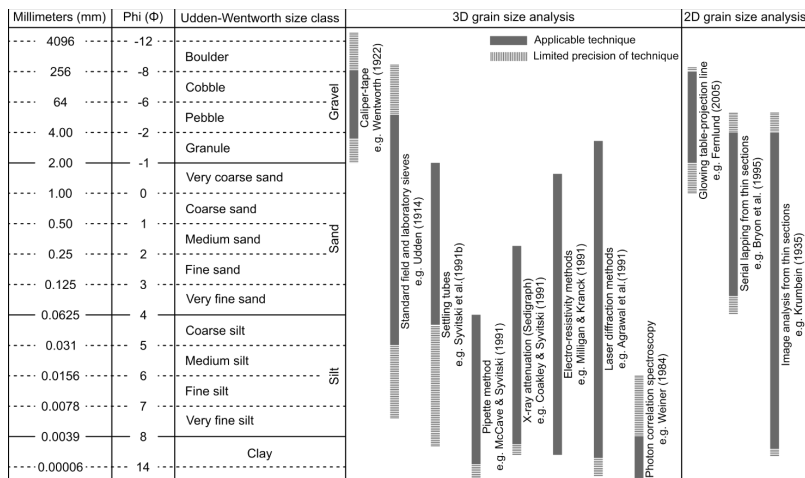
133 provided results matching well with optical granulometry data and proved to be a reliable and
134 an easy-to-use tool to analyze samples with different particle size distributions, textures,
135 sorting degrees, and mineralogical compositions.

Deleted: well matching

136

137 **1.2 Particle size distribution analysis techniques: a review**

138 Since the beginning of the last century, particle size was measured adopting the metric
139 dimensional scale (Wentworth, 1922), which then became the standard sedimentological scale
140 and it is still widely adopted nowadays (Fig. 1). However, in the following years, a base-2
141 logarithm scale, also known as the phi-scale (Φ), was proposed (Krumbein, 1938; Krumbein
142 and Sloss, 1963). Due to the diversity of objects to be characterized, particle size has
143 historically been achieved through the adoption of several methods. The first and simplest
144 employed technique was the direct analysis of particles in the field by caliper or tape
145 measurements (Wentworth, 1922). This methodology was mainly used in the case of coarse-
146 grained materials (coarse gravels, pebbles, cobbles, and boulders), for which size
147 determination was easier, but could not be applied with the same precision to fine-grained
148 media. Sieve analysis has been, and it still is, largely adopted to quickly define the particle size
149 of loose granular media and works well in the case of coarse to medium-grained samples
150 (Udden, 1914; Rosenfeld et al., 1953; Friedman, 1962a; Van Der Plas, 1962; Krumbein and
151 Sloss, 1963; Folk, 1966). However, this method struggles in properly characterizing the size of
152 fine-grained fractions ($< 31-62.5 \mu\text{m}$), which must be analyzed with other, specifically designed,
153 techniques (Krumbein, 1932; Singer et al., 1988; Bianchi et al.,
154 1999) (Fig. 1).



156

157 **Figure 1.** Most common techniques applied in grain size analysis with analytical upper and lower size
 158 boundaries. For a comprehensive literature background of the reported methodologies the reader is referred to
 159 the introduction section 1.2.

160 The adoption of electro-formed sieves may extend the granulometric range down to the fine
 161 silt size (> 5 μm), however this procedure is impractical and requires specifically designed
 162 sieves. Sieving allows the definition of the intermediate axis of particles, considering particles
 163 as anisotropic ellipses, defined by a major (a), intermediate (b) and a minor (c) axis, and can
 164 be used to build mass or volume distribution curves (Bush, 1951; Adams, 1977). Sieving is
 165 typically coupled with sedimentation and pipette analysis to cover the finest (clay and silt-size
 166 particles) fractions of granular samples (Syvitski et al., 1991a; Krumbein and Pettijohn, 1938;
 167 McCave and Syvitski, 1991). However, these techniques may show pitfalls in matching sieving
 168 and sedimentation-pipette results in one single granulometric curve and are also time-
 169 consuming and not suitable to analyze large sample amounts (Syvitski et al., 1991b;
 170 Beuselinck et al., 1998; Bittelli et al., 2019) (Fig. 1). For coarse-grained granular samples (sizes
 171 > 2 mm), image analysis applied to particles or grains manually dispersed on a glowing table
 172 was adopted and the projection of the particle boundaries was used to reconstruct their volume

Deleted: technique



174 and size (Fernlund, 2005). Such a technique proved to be useful in the case of relatively coarse
175 and well disaggregated samples, while it showed limitations dealing with fine-grained or
176 aggregate particles (Fig. 1). The detailed analysis of particle images was implemented also in
177 digital sieving software, coupled with statistical programs (Matlab®), particularly useful to
178 determine the size of loose medium to coarsegrained materials (Kwan et al., 1999; Tafesse et
179 al., 2012). Again, the limitations of this methodology reside in the scarcely representative
180 number of analyzed particles and in the relatively tiny grain size span that can be considered
181 (Fig. 1). In the last decades, the introduction of light diffraction instruments allowed to
182 automatically analyze samples with wide grain size ranges (from clay to gravel) in a single
183 analytical process (de Boer et al., 1987; Agrawal et al., 1991; Blott et al., 2004; Sperazza et
184 al., 2004; Bah et al., 2009). Optical granulometry provides reliable and relatively quick
185 analyses, resulting particularly indicated in the case of numerous samples (Kimura et al., 2018;
186 Brooks et al., 2022). However, reliability of results may depend upon the chosen instrumental
187 parameters, which should be carefully tested to minimize sample alteration (Matthews, 1991;
188 Konert and Vandenberghe, 1997; Blott and Pye, 2006; Storti and Balsamo, 2010; Schulte et
189 al., 2016; Celia Magno et al., 2018; Cortinovis et al., 2019). Moreover, sample treatment, either
190 chemical or mechanical, before the analysis must be conducted carefully to avoid incorrect or
191 biased results (Folk, 1974; McCave et al., 1986; Matthews, 1991; Maithel et al., 2019).
192 Laserdiffraction-based instruments tend to underestimate the clay fraction especially in the
193 case of particles with equivalent diameter finer than 0.1 μm (Sperazza et al., 2004; Brooks et
194 al., 2022). This issue is mainly related to the dispersion medium, and techniques adopted by
195 most of the available equipment, that are not designed to efficiently disaggregate
196 claydominated samples into their constitutive elementary particles (Fig. 1). Techniques relying
197 on electro-resistivity methods, such as the widely used Coulter Counter, measure particle
198 volume based on variations of electrical field induced by grains of different size dispersed in
199 an electrolyte dispersant, which are recorded as electrical pulses with different intensities



200 (Milligan and Kranck, 1991; Beuselinck et al., 1998; Roberson and Weltje, 2014). In a similar
201 way to laser granulometers, electro-resistivity-based instruments have wide applicability in
202 term of particle size but struggle in the clay range ($< 2 \mu\text{m}$) (Fig. 1). X-ray particle attenuation
203 technique (Sedigraph) uses the attenuation of incident radiation caused by sample suspended
204 in a dispersion medium to calculate the concentration of particles settling from suspension
205 (Coakley and Syvitski, 1991; Bianchi et al., 1999; Celia Magno et al., 2018). This method is
206 accurate in analyzing particles with equivalent diameter from 1 to $\sim 300 \mu\text{m}$, while it provides
207 less reliable results outside this grain size interval (McCave and Syvitski, 1991; Cheetham et
208 al., 2008) (Fig. 1). Photon correlation spectroscopy uses the fluctuations of light diffraction
209 generated by Brownian motion of particles suspended in liquid media (Weiner, 1984). This
210 technique is capable of efficiently define the size of particles with equivalent diameter down to
211 1 nm, thus including colloids and is particularly reliable in the clay size range (Fig. 1).

212 The techniques described above are particularly indicated for loose or weakly cemented
213 granular samples that can be easily disaggregated into the elementary constitutive particles.
214 Among the methods involved in particle size analysis in the case of indurated or tightly
215 cemented samples that cannot be easily disaggregated, thin sectioning coupled with
216 petrographic analysis has been the most widely used for decades (Krumbein, 1935;
217 Greenman, 1951; Packham, 1955; Friedman, 1958; Basumallick, 1964; Smith, 1966;
218 Kellerhals et al., 1975; Schäfer and Teysen, 1987; Kennedy and Mazzullo, 1991; Francus,
219 1999; van den Berg et al., 2003) (Fig. 1). Within the thin section area particles accounted for
220 the analysis may be chosen through the grid point count technique (Chayes, 1949;
221 Friedman, 1965; Folk, 1966), the intersection line (Van Der Plas, 1962; Stauffer, 1966) or via
222 manual-automatic identification (Grassy, 1943; Mazzullo and Kennedy, 1985; Kennedy and
223 Mazzullo, 1991; Heilbronner, 2000; Ketcham, 2005; Heilbronner and Barrett, 2014). This latter
224 procedure may be aided by image analysis software (Seelos and Sirocko, 2005; Schneider et
225 al., 2012; Heilbronner and Barrett, 2014; Liu et al., 2021; Théodon et al., 2023). Image analysis



226 techniques can give good results in a wide span of particle sizes, from few mm down to the
227 clay fraction ($\sim 1 \mu\text{m}$), provided that images allow a precise discrimination of fine particles. To
228 this end, image analysis can be performed at several scales of observation spanning from
229 optical microscopy, scanning electron microscopy (SEM) or with transmission electron
230 microscopy (TEM) according to the size of the object to be characterized (Fig. 1). Following
231 thin section cutting, the grain size is determined as the apparent diameter of randomly
232 sectioned particles, which is generally lower than the real or maximum equivalent diameter, a
233 phenomenon known as the corpuscle effect (Wicksell,
234 1925; Rosenfeld et al., 1953; Burger and Skala, 1976; Boggs, 2009; Lopez-Sanchez and
235 Llana-Fúnez, 2016). In order to gain the real and maximum diameter, particles need to be cut
236 along the equatorial diameter, a peculiar configuration that is rather uncommon in sectioned
237 materials (Krumbein and Sloss, 1963). To avoid discrepancy between granulometric data
238 gained from thin section analysis and other methodologies, several correction factors and
239 equations have been developed. Some of them rely on statistical (Chayes, 1950; Burger and
240 Skala, 1976; Kong et al., 2005), stereological (Elias, 1967; Russ, 1986; Sahagian and
241 Proussevitch, 1998; Gallagher et al., 2023), or theoretical-mathematical treatise (Krumbein,
242 1935; Sahu, 1966; Cruz-Orive, 1983), considering particles as perfect spheres randomly cut
243 along the thin section plane. Other correction methodologies apply statistical autocorrelation
244 functions (Panozzo Heilbronner, 1992), software-aided projections of digitized particle outlines
245 (Panozzo Heilbronner, 1983) or empirical correction equations (Harrell and Eriksson, 1979) to
246 compare results from image analysis with data acquired by sieving. Some authors attempted
247 to determine the real grain size distributions by sample serial sectioning to reconstruct the 3D
248 shapes of particles (Bryon et al., 1995; Cooper and Hunter, 1995). Nowadays, there is no
249 univocal Uniquivocal? correlation function linking particle size data from 2D image analysis to
250 the corresponding 3D grain size distributions acquired either by sieving or light diffraction
251 techniques, because all available conversion tools are sample or method sensitive. This

Deleted: grant

Commented [TB1]: Also known as the tomato salad problem or the cut effect.



253 ~~problem prevents~~ a direct comparison between grain size data gained by different analytical
254 techniques.

Deleted: does not allow

255

256 **1.3 A new parameter to match 2D and 3D particle size analyses: volume-weighted** 257 **mean diameter (D_w)**

258 The employed volume-weighted mean diameter (D_w) includes both the equivalent diameter
259 and the shape of analyzed grains. We performed the calculation of volume-weighted mean
260 diameter based on the entire grain size datasets that were extracted from each thin section.

261 The adopted formula operates a weighting of particle diameters according to the volume of the
262 equivalent spheres. Following this, a fine-grained particle influences the final average diameter
263 less than a coarse-grained one. The formula employed for the calculations is:

$$264 \quad D_w = \frac{\sum_{i=0}^{i=n} d_i^3 V_i}{\sum_{i=0}^{i=n} V_i} \quad (1)$$

267 where d_i is the equivalent diameter of the circle having the same area of the traced grains, V_i
268 is the converted spherical volume of grains and i is the number of grains used in the calculation.

269 By developing the formula of spherical volume, equation 1 can be simplified as follows:

$$270 \quad D_w = \frac{\sum_{i=0}^{i=n} \frac{\pi}{6} d_i^4}{\sum_{i=0}^{i=n} \frac{\pi}{6} d_i^3} \quad (2)$$



262 Grain shape was also implemented in the final calculation of the proposed weighted mean
263 diameter. In particular, we considered the deviation of grains from the perfect two-
264 dimensional circular shape. To this aim, we adopted the λ shape correction factor (surface
area correction), which can be calculated from the raw grain size datasets extracted via
image analysis as follows (Johnson et al., 2021):

$$267 \quad \lambda = K * \frac{p_{grain}}{p_{circle}} \quad (3)$$

268 where p_{grain} is the outer perimeter of the manually traced grain boundary and p_{circle} is the
269 circumference of the equivalent circle having the same area of the grain. K is a constant
270 value multiplying the perimeter ratio and can be simplified to 1 in the case of grains with
aspect ratio (elongation of particles) comprised between 1 and 10 (Davies et al., 2019; Song
272 et al., 2020). In calculation of λ shape correction factor we used the average values of grain
273 perimeter and equivalent circle circumference to be inserted in equation 3, considering the
274 entire grain size dataset for each thin section. Following this, we implemented the average
275 λ correction factor in equation 2 to develop the corrected volume-weighted mean diameter
276 formula as indicated below:

$$277 \quad D_w = \lambda * \frac{\sum_{i=0}^n \frac{\pi}{6} d_i^3}{\sum_{i=0}^n \frac{\pi}{6} d_i^3} \quad (4)$$

278

279 4. Analytical methods

280 4.1 Sampled test sandy sediments

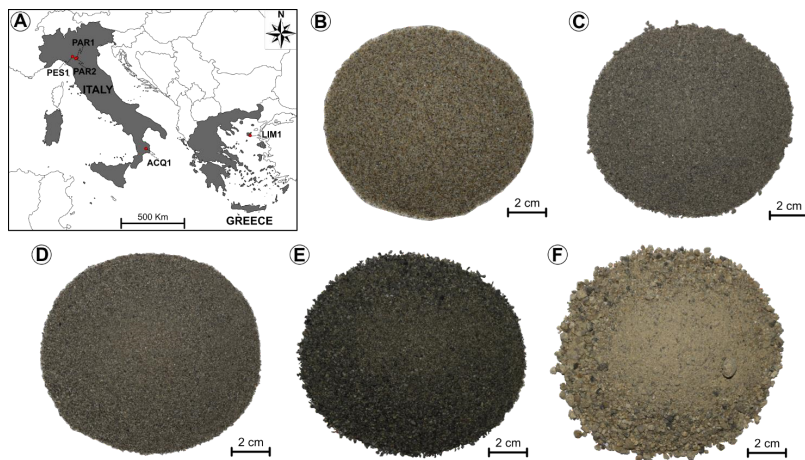
281 We collected 5 different granular sand samples that were used as benchmarks for

<https://doi.org/10.5194/egusphere-2023-2636>
Preprint. Discussion started: 15 November 2023
c Author(s) 2023. CC BY 4.0 License.



282 comparative grain size determinations through thin sections and optical laser granulometer.
283 All samples were characterized by low to no cohesion and were easily collected by hand or

283 with sampling tools. About 500 g of sandy materials were collected. Sand specimens belonged
284 to different sedimentological environments spanning from continental-fluvial (braided stream
285 rivers) to shallow marine (beach and deltaic settings) (Fig. 2a).



286

287 **Figure 2.** Geographical position and pictures of collected sand samples. (a) Central and Eastern Mediterranean
288 Sea area showing the position of collected samples. (b) Sample amount LIM1 beach sand from Lemnos Island,
289 NE Greece. (c) Sample amount PAR1 from the bottom of a fluvial sand bar collected in the Parma Creek,
290 Northern Apennines. (d) Sample amount PAR2 from the top of a fluvial sand bar collected in the Parma Creek,
291 Northern Apennines. (e) Sample amount PES1 fluvial sand from the Pessola Creek, Northern Apennines. (f)
292 Sample amount ACQ1 deltaic sand from fossil fluvial-shallow marine setting from Crotona Basin, Southern
293 Apennines.

294 Sampling strategy was aimed to collect sands with different modal compositions, average grain
295 sizes and grain size distributions (different sorting degree, modal peak, curve shape and
296 asymmetry). In particular, sample LIM1 was collected in a recent foreshore swashing zone
297 along the eastern coast of Lemnos Island in the North Aegean Sea, Greece. The beach sand
298 is medium-grained, well sorted, and displays high-textural maturity with rounded to subrounded
299 grains mainly composed of quartz and lithic fragments (Fig. 2b). Three sand specimens were
300 sampled from different braided stream type, creeks, of Northern Apennines in North Italy, with



301 samples PAR1 and PAR2 representing the bottom and the top of a recent fluvial sand bar along
302 the Parma Creek, respectively. The sand bar is interfingered with coarse gravel and boulder-
303 cobble bodies. The sand samples are fine to medium-grained, with moderate sorting degree,
304 fair textural maturity with subrounded grains composed of quartz, feldspar, and silt-clay
305 aggregates (Fig. 2c and d). Conversely, PES1 sample was collected at the base of a recent
306 slope debris talus slightly reworked by stream current along the Pessola Creek in the Northern
307 Apennines. The sand exhibits medium to coarse grain size, moderate to poor sorting, and low
308 textural maturity indicated by subrounded to subangular grains mainly composed of lithics and
309 subsidiary quartz and feldspar (Fig. 2e). Finally, ACQ1 sand sample was collected from a
310 Lower Pliocene age deltaic sandstone bar from the Crotona Basin in South Italy. Although this
311 sample belongs to a fossil siliciclastic deposit, the sandstone is almost devoid of any diagenetic
312 cements, thus allowing an easy sampling. This fluvial-deltaic sandstone is coarse-grained,
313 poorly sorted and displays low textural maturity, with subangular feldspar grains dominating
314 with respect to rock fragments and quartz (Fig. 2f).

Deleted: Eventually

315

316 **4.2 X-ray diffraction mineralogical analysis**

317 The detailed analysis of the mineralogical composition of sampled sands was achieved through
318 X-Ray Powder Diffraction (XRPD) technique. Before the analyses, all samples were dried at
319 the controlled temperature of 35 °C for 48 hours and representative sand amounts (~2 g) were
320 manually milled in a jade mortar to attain an average grain size < 63 µm. A Bruker D2 Phaser
321 powder diffractometer with θ - θ focalizing geometry was used, operating at 30 kV and 10 mA
322 with Cu-K α ($\lambda = 1.54178 \text{ \AA}$) radiation. Data were collected in the 5-60° 2 θ angular range, with
323 0.02° step size and 1 s/step counting time. Each sample was spun at 30 rpm. To identify the
324 crystalline phases EVA software (Bruker EVA, 2018) and the Crystallography Open Database
325 (COD) were used. Semi-quantitative analysis of the detected mineralogical phases was



327 conducted using the RIR method, adding a 10 wt% high purity Si standard in each sample.
328 Through the adoption of semi-quantitative technique, the identification of clay minerals through
329 emission peak position cannot be considered exhaustive. Further investigation and analysis of
330 samples under different conditions (dry, heated, and swollen) would be required for a precise
331 clay mineral identification but such in-depth analysis falls beyond the scope of the present
332 study.

333

334 4.3 Laser-diffraction grain size analysis

335 All granular samples were dried in an oven at the controlled temperature of 40 °C for two days
336 to remove most of the water content. After sample drying, the total amount (~500 g) was sieved
337 with a 2,000 µm mesh to remove grains with equivalent diameter coarser than 3,500 µm, which
338 represents the upper instrumental limit of the laser granulometer. By doing this, we slightly
339 restricted the original grain size distribution of all samples, removing fine gravel sized grains.
340 The alteration by sieving of original grain size distribution was the same for all samples. The
341 original sample amounts were split in aliquots using Quantachrome Instruments macro and
342 micro riffers to achieve the sample mass required for grain size analysis (0.8-1.3 g) (Fig. 3a).

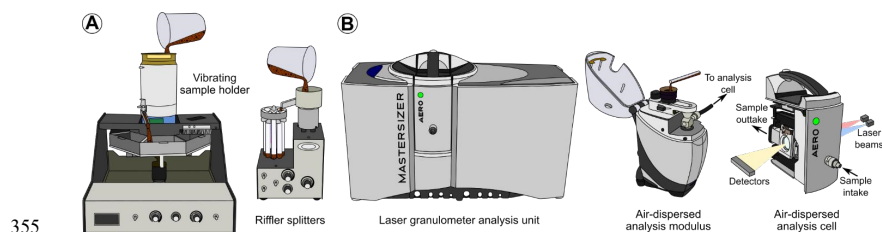
343 This process also allowed creation of sub-samples still preserving the original grain size
344 distribution of the total starting sample amount. Grain size analyses were performed with a
345 Malvern Panalytical Mastersizer 3000 optical granulometer, with operating size range spanning
346 from 10 nm to 3,500 µm (Fig. 3b). The instrument was equipped with an Aero S air-dispersed
347 analysis unit, using pressurized air as particle dispersant medium (Fig. 3b). The adoption of air
348 as dispersant allowed to analyze samples minimizing the alteration and mechanical
349 disaggregation operated by commonly used liquid dispersant media (distilled water or alcohol).

350 For all five analyzed samples, a specific standard operating procedure was set to give the most
351 reliable and reproducible analysis.

Deleted: to

Deleted: also to create

Deleted: grant



355

356 **Figure 3.** Instrumental apparatus and sample preparation used to perform laser diffraction analysis. (a) Macro
357 and micro rifflers necessary to split the initial sample amount in sub-samples suitable to be inserted in the laser
358 granulometer and to be dedicated to thin sectioning. (b) Mastersizer 3000 laser granulometer optical unit,
359 equipped with an Aero S air-dispersion modulus with the dedicated analysis cell designed to work on incohesive
360 granular media.

361 The operating procedures included several analytical-instrumental parameters to be set prior
362 to the definitive analysis. In our analyses, the granular sample quantity, laser power
363 obscuration, negative air pressure and feed rate were carefully tested (details are provided in
364 Supplementary material 1). The granulometer has two different light sources producing two
365 laser beams with red (632.8 nm) and blue (470 nm) wavelength, respectively (Fig. 3b).
366 Calculation of the equivalent grain diameter was made via a light diffraction law, employing the
367 Mie light scattering theory, which requires the refractive and adsorption indexes of particles.
368 Our granular materials are multi-dispersed (particles with different size and shape) mixtures of
369 several mineralogical phases including quartz, K-feldspar, plagioclase, mica, and rock
370 fragments in different proportions. Nevertheless, we adopted the optical parameters of
371 crystalline quartz, which is the most abundant mineral phase, with diffraction index of 1.54 and
372 adsorption index of 0.1. This simplification was needed because the granulometer is not
373 designed to work on complex polymineralic assemblages. Particle volume was back-calculated
374 from light diffraction scattering distribution and, under the



373 assumption of perfect spherical objects, the equivalent diameter was calculated. Optical
 374 diffraction is operated differently according to grain size, with fine particles producing wide
 375 light scattering angles, while coarse grains induce low angles (Brooks et al., 2022). The
 376 laser granulometer performs the calculation of equivalent grain diameter adopting the 377
 method of moments as indicated in the generic formula below:

$$378 \quad D[m, n] = \frac{1}{\left(\frac{\sum_{i=0}^{\infty} V_i d_i^{m+n}}{\sum_{i=0}^{\infty} V_i d_i^m} \right)^{\frac{1}{n}}} \quad (5)$$

379 in which V_i stands for particle volumetric density in size class d_i (median value of grain size
 380 class), while m and n are the exponents to be substituted with different indexes according
 381 to the adopted method of moments. In our case, the granulometer calculates the volume382
 weighted mean diameter (De Broucker mean diameter or D[4:3]), adopting as indexes m
 383 and n in equation 5, 4 and 3, respectively. The granulometer also provides the span, or the
 384 width of the grain size distribution curves calculated at half height of modal peak, according
 385 to the formula:

$$386 \quad Span = d \frac{d(x,0.9) - d(x,0.1)}{d(x,0.5)} \quad (6)$$

387 where, d is the equivalent particle diameter value at 0.1, 0.5 and 0.9 thresholds of the grain
 388 size distribution, and x can be substituted according to the distribution type adopted during
 389 the analysis (number or volume of particles). Optical granulometric analyses were replicated
 390 on 5 aliquots of each sample. Grain size distribution curves were averaged to obtain mean
 391 grain diameters and related parameters with associated standard deviations.

392

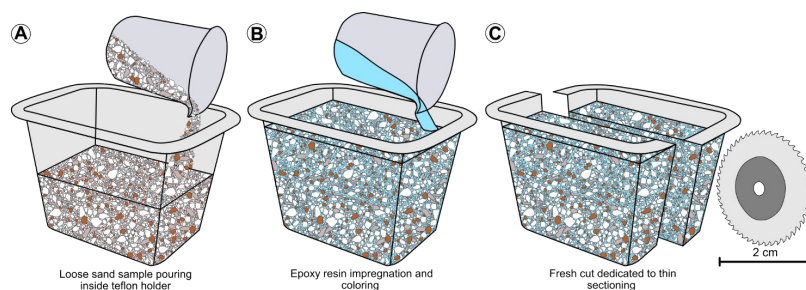
<https://doi.org/10.5194/egusphere-2023-2636>
Preprint. Discussion started: 15 November 2023
c Author(s) 2023. CC BY 4.0 License.



393 **4.4 Thin sectioning technique of loose sand samples**



393 Petrographic thin sections having thickness of 30 μm were made from granular sand samples.
394 To prevent any preferential grain orientation and to preserve the original grain size distribution,
395 all samples were split with macro and micro riffers, and several aliquots were added into Teflon
396 containers (Fig. 4a).



397

398 **Figure 4.** Sample preparation before thin sectioning. (a) Sample pouring inside Teflon holder after being split in
399 representative sub-samples with vibrating riffers. (b) Granular sample impregnation with a mixture of Araldite
400 resin and Prochima Pentasol blue dye. (c) Precise saw-cutting along the vertical direction, with thin section
401 made along the fresh cut.

402 Typically, 20–28 g of loose sand were used to fill $4 \times 3 \times 2.5$ cm Teflon sample holders, with
403 mass variations due to different sample density and grain size. Loose sand samples were
404 impregnated with a mixture of Araldite BY156 epoxy resin and Aradur 21 resin hardener (resin-
405 hardener mass proportion of 100:28), which was diluted to 10% of total volume with ethyl
406 acetate to grant lower viscosity. The mix was colored by adding a Prochima Pentasol (UN) blue
407 dye with a mass equal to 6% of the Araldite resin (Fig. 4b). The coloring provided a uniform
408 light blue background which helped in identifying grains and tracing grain boundaries.
409 Indurated samples were cut vertically, and the fresh cut was used to create petrographic thin
410 sections (Fig. 4c). Thin rock slices were glued onto transparent glass using an Epoteck 301
411 epoxy resin mixed with Aradur 21 hardener (resin-hardener mass proportion of 20:5). Finally,
412 thin sections were manually polished with polycrystalline synthetic diamond powder, having a

Deleted: adopting

Deleted: Eventually



415 grain size of 1 μm , above a Tanganyika soft wooden surface. The polishing procedure was
416 needed to precisely identify grain mineralogy, to detect grain outer boundaries and to increase
417 the overall thin section transparency and quality.

418

419 **4.5 Sand sample modal composition**

420 The definition of the modal composition of sand samples was obtained by means of
421 petrographic analysis, with recognition of the principal mineralogical phases (quartz, feldspar,
422 and lithic fragments) in thin section. Quantification of areal percentage of minerals was done
423 on high resolution photomicrographs acquired with a Zeiss Axioplan 2 petrographic
424 microscope, equipped with a Leica MC 170 HD high sensitivity camera. Photomicrographs
425 were acquired at 12.5 \times magnifications (picture area of 4,747 \times 3,560 μm) both under plane
426 and cross polarized light, to ease mineral identification. A total of 5 dedicated photomicrographs
427 were taken and analyzed for each sample. Sand samples were classified adopting the
428 standard Q-F-L ternary classification diagram used for sandstones (Folk, 1974).

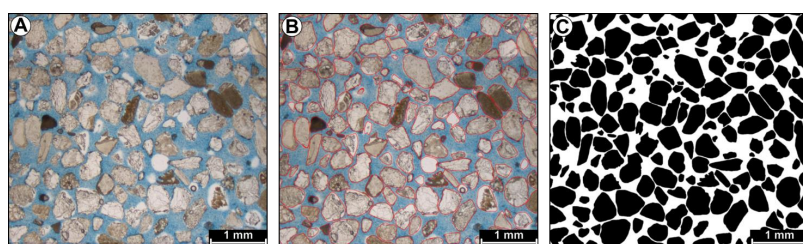
429

430 **4.6 Particle size analysis through 2D image analysis**

431 The analysis of grain size via image analysis on thin section was performed on petrographic
432 photomicrographs acquired with the standard microscope setting described above. For each
433 thin section, 48 to 64 photomicrographs were taken at 12.5 \times magnifications (picture area of
434 4,747 \times 3,560 μm) under plane polarized light to cover the entire thin section area and were
435 stitched together to form photomosaics. Photomosaics were imported and calibrated in ImageJ
436 image analysis, open-source software (Schneider et al., 2012). Little processing was required



437 to enhance image quality mainly through brightness-contrast adjustments and noise-outlier
438 pixel removal (Fig. 5a).



439

440 **Figure 5.** Image analysis technique adopted to obtain 2D particle size distribution from the selected samples.
441 (a) Original photomicrograph acquired at 12.5× magnification, composing the analyzed photo-mosaics. (b)
442 Results of manually traced particle outer boundaries. (c) Transformed binary (black and white) photomicrograph
443 used to extract particle equivalent diameter.

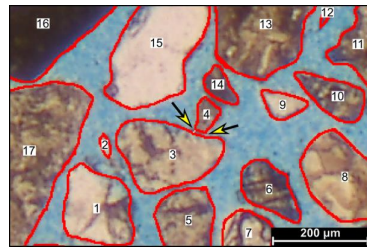
444 Grains were traced on modified photomosaics with ImageJ manual tracing tool, taking care to
445 keep a constant 2-pixel width of the traced boundaries (Fig. 5b). After digitization, grains were
446 identified by the software with color thresholding technique applied to red grain boundaries and
447 photomosaics were converted to binary images (black grains on white background) (Fig. 5c).

Deleted: having

448 Special attention was paid to drawing grain boundaries, to avoid grains in contact with each
449 other. In the case of touching grains, instead of operating image segmentation, we preferred
450 double-checking the results to find errors and mistakes during tracing, that were corrected by
451 manual separation of grains adding different color pixels (Fig.

Deleted: in

452 6).



454

455

Figure 6. Double-checking of grains in contact with each other. Final digitized photo-mosaics quality check to 456 identify tangent grains which were manually segmented by adding pixels with different color from the red 457 particle outline (yellow arrows).

458

After image correction, grain size-shape data were extracted. For grain size, we extracted

459

the area fraction in μm^2 of grains which were approximated to perfect circles, and the 460

equivalent diameters were calculated from the inverse formula of the circle's area (Fig. 7):

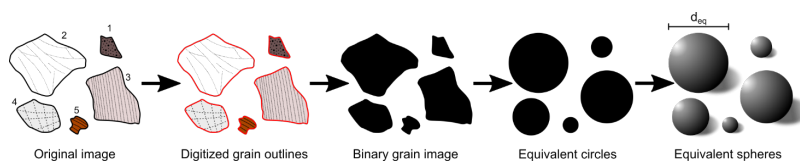
461

$$d_{eq} = 2 * \sqrt{\frac{A}{\pi}} \quad (7)$$

462

where d_{eq} is the equivalent diameter of the circle having the same area of the particle and A

463 is the real area of the particle measured with image analysis.



464

465

Figure 7. Sequence of progressive steps to perform manual image analysis and to extract particle equivalent 466 circles and spheres. d_{eq} , equivalent particle diameter.

467

Values extracted from this formula composed the basis of the proposed volume-weighted

468

mean diameter. A total of 133,372 grains were considered and typically more than 5,000



469 grains were used in each thin section. Large datasets allowed to tune the volume-weighted
470 calculation formula and to minimize the effect of random grain sectioning (Krumbein, 1935;
471 Friedman, 1958; Kellerhals et al., 1975; Kong et al., 2005). Grain size distributions
were
472 created from the conversion of particle number into volume density percentage associated
473 with each grain size bin. Conversion was made considering the total volume of spherical
474 shape grains divided according to the instrumental grain size classes adopted by the laser
475 granulometer. By doing this, we kept the same boundary and instrumental conditions for
476 both grain size data acquired through laser granulometry and image analysis, facilitating the
477 comparison.

478 Regarding grain shape, aspect ratio (AR) was calculated and used to describe the deviation
479 of grains with respect to the perfect circle. Aspect ratio was obtained by the formula:

$$480 \quad AR = \frac{Major \text{ axis}}{Minor \text{ axis}} \quad (8)$$

481 where *Major axis* indicates the longest axis of the particle best fit ellipse (segment
482 connecting the two farthest points along the grain perimeter) and *Minor axis* stands for the
483 shortest axis of the best fit ellipse (segment having as tips the two closest points along the
484 grain perimeter).

485

486 **5. Main results**

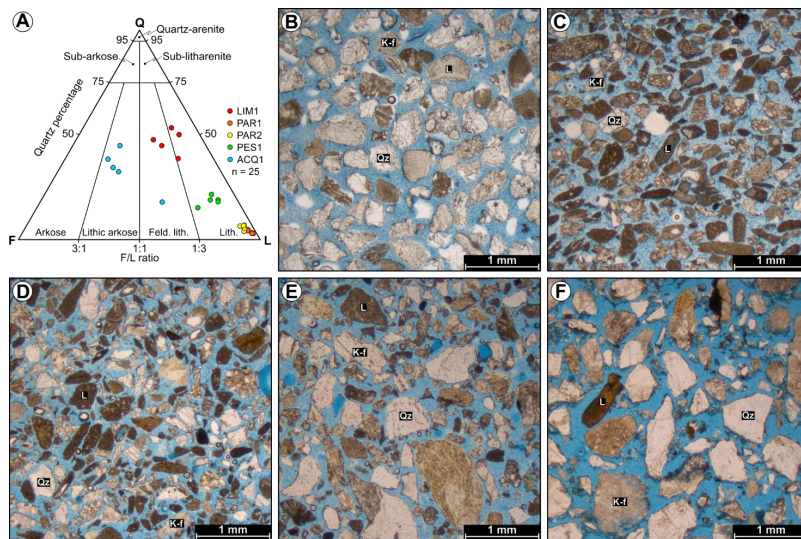
487 **5.1 Petrographic-mineralogical sample description**

488 Micro-textural and modal analyses performed on the foreshore beach sand sample (LIM1),
489 point out a mineralogical composition made of almost equal proportions of quartz (38.81-490
53.32%) and lithic fragments (32.05-46.8%), while feldspar and plagioclase are subordinate



491 (8.37-20.17%) (Fig. 8a and b). Lithic fragments are mainly composed of calcite-aragonite
492 bioclasts, peloids, and to a lesser extent of metamorphic and igneous rock fragments. This
493 sample plots between the feldspathic litharenite and litharenite compositional fields in the

493 Q-F-L classification diagram (Fig. 8a). Grains are rounded to subrounded, with quartz being
494 more equant than feldspar and lithics which appear more elongate. Sorting degree is high with
495 grains of different mineral composition showing similar overall size.



496
497 **Figure 8.** Micro-textural characteristics and mineralogical composition of the collected sand samples. (a)
498 Ternary Quartz-Feldspar-Lithics modal classification diagram reporting the composition of studied sands (Folk,
499 1974). Sand composition was calculated from 5 photomicrographs per each sample. (b) Rounded to
500 subrounded siliciclastic and biogenic particles composing LIM1 beach sand sample. (c) Subrounded and
501 elongate lithic-dominated grains of PAR1 fluvial sample. (d) Subrounded lithic-dominated particles with lesser
502 extents of quartz and feldspar composing PAR2 fluvial sample. (e) Subangular and poorly sorted fluvial sand of
503 PES1 sample. (f) Angular to subangular, poorly sorted fluvial-deltaic sand composing ACQ1 sample. Q, quartz;
504 K-f, feldspar; L, lithic fragment; n, number of used photomicrographs.

505 The sand sample collected along the base of a fluvial bar (PAR1), displays a completely
506 different mineral assemblage compared to the beach sand. In particular, the modal analysis
507 returns a high lithic percentage (92.75-95.74%), while quartz (3-4.51%) and feldspar
508 (1.252.86%) compose the remaining areal amounts of the sample (Fig. 8a, c). Lithics have a
509 sedimentary origin with silt-clay aggregates incorporating fine-grained quartz and feldspar

Deleted: S

Deleted: latter



512 particles to produce coarse-grained aggregates. The fine-grained matrix of aggregates is
513 dominantly composed of muscovite and chlorite-group minerals, as confirmed by XRD
514 analysis. Metamorphic and igneous fragments are present as subordinate mineral
515 components. Due to the high lithic content, PAR1 sample can be inserted in the litharenite field
516 in the Q-F-L ternary diagram, close to the 100% lithic endmember (Fig. 8a). Grains are
517 generally subrounded, with lithics exhibiting more anisotropic shapes with smooth outer
518 boundaries, while quartz grains are subangular with rougher boundaries. The sorting degree
519 is average with grains covering different grain size classes.

520 The sample from the top of the fluvial bar (PAR2), shows a mineral composition close to the
521 underlying PAR1 previously described, with lithics dominating with respect to quartz and
522 feldspar. Lithic fragments compose most of the areal percentage of the sample (88.6591.36%),
523 while quartz (4.01-6.72%) and feldspar-plagioclase (3.22-4.84%) are subordinate (Fig. 8a, d).
524 Lithics are mainly made of sedimentary aggregates of silt and clay-sized particles (muscovite
525 and chlorite), but a lesser content of metamorphic rock fragments occurs (polycrystalline quartz
526 grains). This sample can be inserted in the litharenite, lithicdominated field in the Q-F-L ternary
527 diagram, next to PAR1 sample (Fig. 8a). Lithic fragments are subrounded with highly elongate
528 shapes and smooth boundaries. Conversely, quartz grains are subangular to angular with
529 marked asperities and edges along the outer boundaries. Feldspar and plagioclase are
530 subrounded and grains display smooth perimeters. The sorting of the sample is average with
531 a considerable span through grain size classes.

532 The fluvial-reworked talus debris sample (PES1) is characterized by a mineral composition
533 shifted towards lithics, with considerable amounts of quartz and feldspar. Again, lithic
534 fragments constitute more than half of the sample (66.44-73.57%), followed by quartz (15.5-
535 21.62%) and feldspar-plagioclase (7.96-18.05%) (Fig. 8a, e). Most of lithics are composed of
536 ultramafic rock fragments (basalts, peridotites and gabbros), with lesser contribution from



537 metamorphic, hydrothermally altered rocks (serpentinites). Sedimentary lithic aggregates of
538 silt and clay, encasing siliciclastic particles, occur. The fine-grained matrix forming aggregates
539 is composed of clay minerals as documented by XRD analysis (Supplementary material 2).
540 According to the Q-F-L ternary diagram, PES1 sample can be ascribed to the litharenite field,
541 although slightly enriched in quartz and feldspar with respect to PAR1 and PAR2 (Fig. 8a).
542 Lithic fragment shape varies from subrounded to angular, with very rough outer boundaries.
543 Feldspar grains show subrounded and isotropic crystal form, while quartz has subangular to
544 angular shape. The sorting degree is poor, with particles displaying a wide grain size span.

545 Finally, the sand sample collected from the deltaic sandstone bar (ACQ1) displays a mineral
546 composition with similar percentage of feldspar, quartz and lithics. In this sample, feldspar and
547 plagioclase compose most of the sample (31.58-43.81%), followed by quartz (18-44.83%) and
548 lithic fragments (17.9-50.41%) (Fig. 8a, f). Lithics have different composition, with igneous-
549 intrusive terms (granites) dominating with respect to metamorphic (schists-gneisses) and
550 sedimentary ones (sandstones). Feldspar and plagioclase crystals are severely affected by
551 alteration to sericite minerals (muscovite and paragonite). ACQ1 sample can be inserted in the
552 lithic arkose field of the Q-F-L classification diagram (Fig. 8a), although one of the used
553 photomicrographs falls in the feldspathic litharenite field due to the heterogeneous distribution
554 of several coarse feldspar grains. Feldspar grains have subrounded shapes, while quartz is
555 subangular to angular. Lithic fragments of igneous origin have subangular shapes with rough
556 outer boundaries, while sedimentary lithics are subrounded and more elongate, with smooth
557 boundaries. The sorting degree is low, with a wide span of grain size classes.

Deleted: Eventually

558

559 **5.2 Laser-diffraction grain size analysis**

560 Optical granulometry grain size analyses on loose samples were replicated with 5 aliquots of
561 equal mass, and the grain size distribution curves were averaged to obtain a mean grain



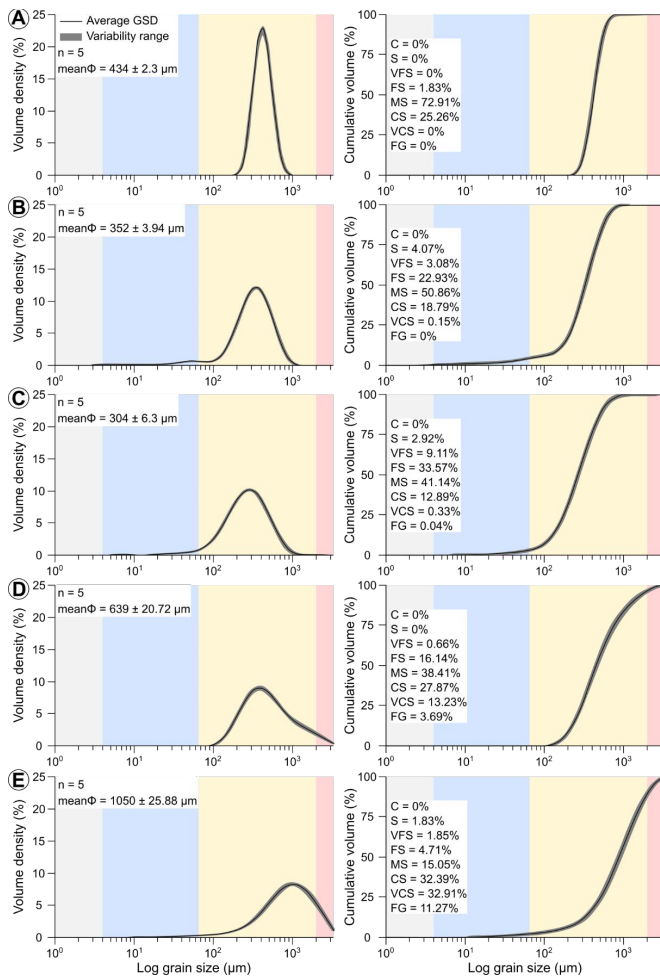
563 diameter value and related parameters. The following results are presented considering the
564 calculated average grain size distribution curve for each sample.

565 5.2.1 Beach sand sample (LIM1)

566 LIM1 sample displays a narrow grain size distribution curve, with subtle positive asymmetry.
567 The grain size distribution has intercepts with the X axis at 174 and 1,041 μm , respectively.
568 The calculated average grain diameter is $434 \pm 2.3 \mu\text{m}$, with a modal value of $419 \pm 1.9 \mu\text{m}$
569 and a median of $420 \pm 1.9 \mu\text{m}$ (Fig. 9a). The span of grain size distribution is low (good sorting
570 degree) with an average value of 0.665 ± 0.01 . All grains fall in the sand grain size interval with
571 the most recurrent size class being the medium-grained sand with 72.91% of particle volume
572 density. Coarse-grained particles compose 25.26% of the total sample volume, while the
573 remaining 1.83% is due to the fine-grained sand fraction (Fig. 9a).

574 5.2.2 Basal fluvial sand bar sample (PAR1)

575 The sand sample collected along the basal surface of a fluvial sand bar along the
576 braidedstream Parma Creek (PAR1), is characterized by an average grain size distribution
577 curve with medium width showing positive asymmetry. The left (finer) tail of the distribution
578 curve is more pronounced than the right (coarse) one with particles being detected at 2.9 μm
579 on the fine-ward side. Conversely, the right tail of the grain size curve intercepts the X axis at
580 1,182 μm . The average particle diameter is $352 \pm 3.9 \mu\text{m}$, with a modal value of $350 \pm 1.9 \mu\text{m}$
581 and a median of $328 \pm 2.6 \mu\text{m}$ (Fig. 9b). Grain size distribution span is higher than the one
582 shown by the previous sample and the calculation returns a mean value of 1.343 ± 0.02 . The
583 most recurrent grain size class is the medium-grained sand with 50.89% of particle volume
584 density. Fine-grained and coarse-grained classes compose 22.93% and 18.79% of the total
585 sample volume, respectively. Minor amounts of volumetric densities are measured in the silt
586 size (4.07%), very fine-grained sand size (3.08%), and in very coarse-grained sand size
587 (0.15%) (Fig. 9b).



588

589 **Figure 9.** Grain size distribution curve obtained through laser granulometer analysis. (a) Volume density and
 590 cumulative distribution for LIM1 sample. (b) Volume density and cumulative distribution for PAR1 sample. (c)
 591 Volume density and cumulative distribution for PAR2 sample. (d) Volume density and cumulative distribution for
 592 PES1 sample. (e) Volume density and cumulative distribution for ACQ1 sample. GSD, grain size distribution; Φ
 593 particle diameter; n, number of analyses; C, clay; S, silt; VFS, very fine-grained sand; FS, finegrained sand; MS,
 594 medium-grained sand; CS, coarse-grained sand; VCS, very coarse-grained sand; FG, fine gravel.



595 *5.2.3 Upper fluvial sand bar sample (PAR2)*

596 The medium-grained sand collected on the top surface of a sandy bar along the Parma Creek
597 (PAR2), displays an average grain size distribution curve with medium width and slight positive
598 skewness. On the left tail, finest particles are recorded at $4.9\ \mu\text{m}$, while on the right tail coarsest
599 grains are detected at $1,343\ \mu\text{m}$. The calculated average grain diameter is $304 \pm 6.3\ \mu\text{m}$, with
600 a mode at $286 \pm 3.3\ \mu\text{m}$ (Fig. 9c). The span of the average grain size curve is higher than
601 previous samples, with a mean value of 1.608 ± 0.03 and a median of $267 \pm 2.7\ \mu\text{m}$. Higher
602 span is recorded also by the particle volume distribution, with 41.14% of grains falling in the
603 medium-grained sand class and 33.57% of grains composing the finegrained sand size. A
604 considerable volume of particles falls in the coarse-grained sand size (12.89%), while only a
605 small fraction is recorded in the very coarse-grained sand (0.33%) and fine gravel grain size
606 classes (0.04%). On the fine-ward side, no clay-sized particles are recorded, while silt-size and
607 very fine-grained sand classes compose 2.92% and 9.11% of the total sample volume,
608 respectively (Fig. 9c).

609 *5.2.4 Fluvially-reworked debris talus sand sample (PES1)*

610 The medium to coarse-grained sand sample collected from a debris talus reworked by river
611 stream (PES1) is characterized by an average grain size distribution curve with high width and
612 strong positive asymmetry. Grain size distribution tails are not symmetric, with the left one
613 being steeper than the right tail. On the left tail, finest grains are recorded at $81\ \mu\text{m}$, while on
614 the right tail coarsest particles reach $3,300\ \mu\text{m}$ of equivalent diameter. The average grain
615 diameter gained from the mean curve is $639 \pm 20.72\ \mu\text{m}$, with a modal value of $386 \pm 2.41\ \mu\text{m}$
616 and a median of $455 \pm 8.6\ \mu\text{m}$ (Fig. 9d). The span of average grain size curve is higher than
617 the samples described before, with a mean value of $2.495 \pm 0.11\ \mu\text{m}$. Higher span can be
618 traced also in the volumetric particle distribution among grain size classes. In particular, the
619 dominant grain size class is the medium-grained sand size with 38.41% of volume density.



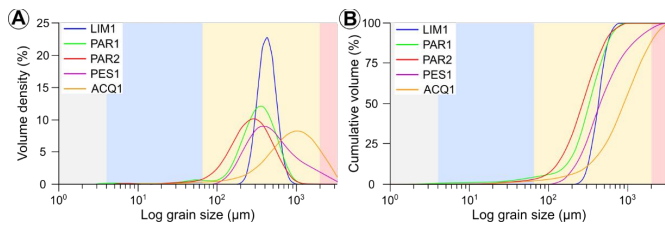
620 Relatively high particle volumes are recorded also in the coarse-grained sand (27.87%), fine-
621 grained sand (16.14%) and in the very coarse-grained sand classes (13.23%). Minor amounts
622 of grains can be detected in the fine gravel class (3.69%) and in the very fine-grained sand
623 range (0.66%) (Fig. 9d).

624 5.2.5 Deltaic sand sample (ACQ1)

625 The coarse-grained sandstone collected along an exposed fossil deltaic bar (ACQ1) displays
626 a wide grain size distribution curve with a weak positive asymmetry. The average curve shows
627 asymmetric tails, with a steep right tail (coarse) and a gentle left tail (fine).

628 Finest particles are recorded at 8.1 μm , while coarse ones have equivalent diameters of
629 3,300 μm . The average equivalent grain diameter is $1,050 \pm 25.88 \mu\text{m}$, with a mode of $1,020 \pm$
630 $57.92 \mu\text{m}$ and a median of $897 \pm 27.1 \mu\text{m}$ (Fig. 9e). The span shown by the mean granulometric
631 curve is equal to $1.993 \pm 0.02 \mu\text{m}$, slightly lower than PES1 sample. Data regarding single
632 grain size classes point out the high curve width. In this sample is difficult to identify a single
633 dominant grain size class, since coarse and very coarse-grained classes compose 32.39%
634 and 32.91% of total volumetric particle density, respectively. Considerable particle amounts are
635 also displayed by medium-grained sand (15.05%) and fine gravel size classes (11.27%). Minor
636 volumetric densities are recorded in fine-grained sand range (4.71%), very fine-grained sand
637 class (1.85%) and in the silt grain size interval (1.83%). No grains have been measured in the
638 clay-sized fraction (Fig. 9e).

639 To summarize, from sample LIM1 to ACQ1 we record a coarsening of average grain diameter,
640 a general broadening of grain size distribution curves (decrease of sorting degree), and a more
641 marked asymmetry between left and right tails of the curves (Fig. 10a and table 1). The same
642 observations can be made checking the cumulative grain size distributions, which show a
643 progressive decrease of slope following an increase of grain size (Fig. 10b and table 1).



644

645 **Figure 10.** Comparison of grain size distribution obtained with air-dispersed laser granulometer. (a) Volume
 646 density grain size distributions. (b) Cumulative volume percentage grain size distributions.

647

648

Table 1: Summary of analytical parameters extracted from laser granulometry analyses

Sample name	Sample type	Age	D _m (µm)	D _{x10} (µm)	D _{x50} (µm)	D _{x90} (µm)	Mode (µm)	Span
LIM1	Foreshore beach sand	Recent	434 ± 2.3	303 ± 1.87	420 ± 1.92	582 ± 4.15	419 ± 1.94	0.665 ± 0.01
PAR1	Base of fluvial sand bar	Recent	352 ± 3.94	152 ± 1.48	328 ± 2.61	593 ± 9.76	350 ± 1.92	1.343 ± 0.02
PAR2	Top of fluvial sand bar	Recent	304 ± 6.3	115 ± 1.34	267 ± 2.68	545 ± 12.18	286 ± 3.29	1.608 ± 0.03
PES1	Talus debris reworked along river	Recent	639 ± 20.72	211 ± 1.92	455 ± 8.62	1350 ± 71.55	386 ± 2.41	2.495 ± 0.11
ACQ1	Deltaic sandstone bar	Lower-Middle Pliocene	1050 ± 25.83	283 ± 8.02	897 ± 27.14	2070 ± 40.86	1020 ± 57.92	1.993 ± 0.02

649

650 **Table 1.** Summary of grain size analysis via laser granulometry. D_m, average particle diameter; D_{x10}, D_{x50}, D_{x90},
 651 grain size thresholds (percentiles) at 10, 50 and 90% of particle volume distribution.

652

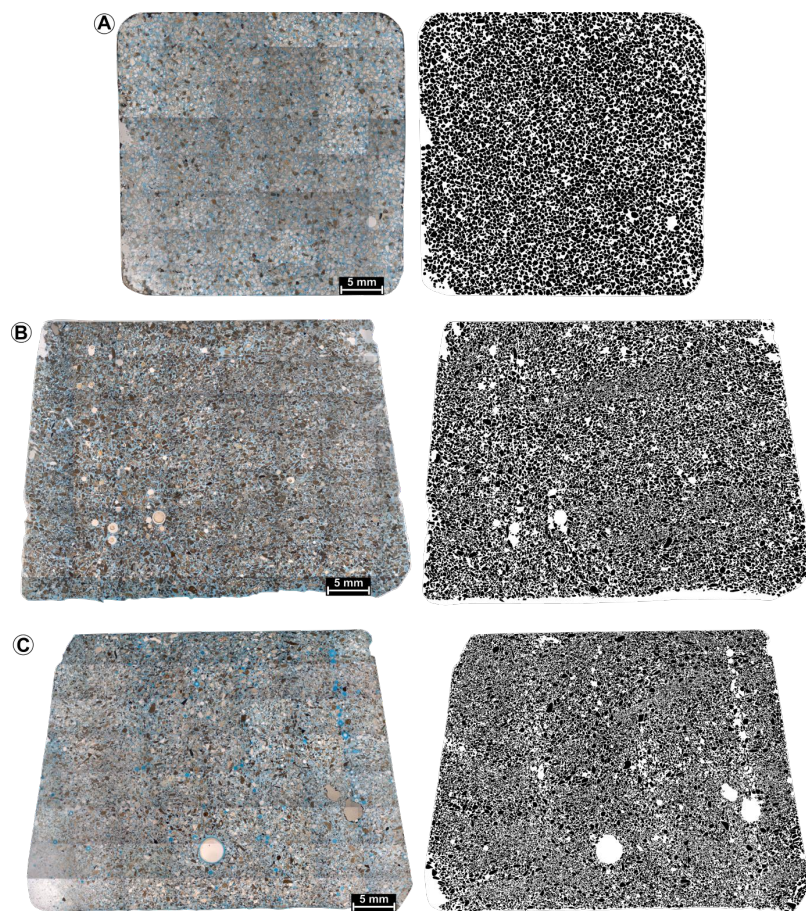
653 5.3 Thin section-image analysis grain size distributions

654 Two-dimensional grain size analysis was based on data gained from petrographic thin sections
 655 analyzed through image analysis technique. All grains composing the thin sections were
 656 digitized to provide robust datasets which served to set the 3D volume-weighted mean
 657 diameter conversion formula (Fig. 11). 5.3.1 Beach sand sample (LIM1)

658 For the foreshore-beach sand sample LIM1, a total of 5,419 grains were acquired (Fig. 11a).
 659 The resulting particle number grain size distribution curve has intercepts with the X axis at 40
 660 and 756 µm and a mode of 352 µm. The volume density converted distribution shows a roughly



661 symmetric bell shape with a weak skew towards finer particles and a modal value of 390 μm
662 (Fig. 12a). The sorting degree is high as testified by most of the grains falling in the medium-
663 grained sand size class (87.54%), while lesser particle amounts are recorded in the fine-
664 grained sand (6.89%) and in the coarse-grained sand intervals (5.29%). Only small fractions
665 of silt-sized and very fine-grained sand material were detected, with percentage of 0.01% and
666 0.26%, respectively (Fig. 12a).



667

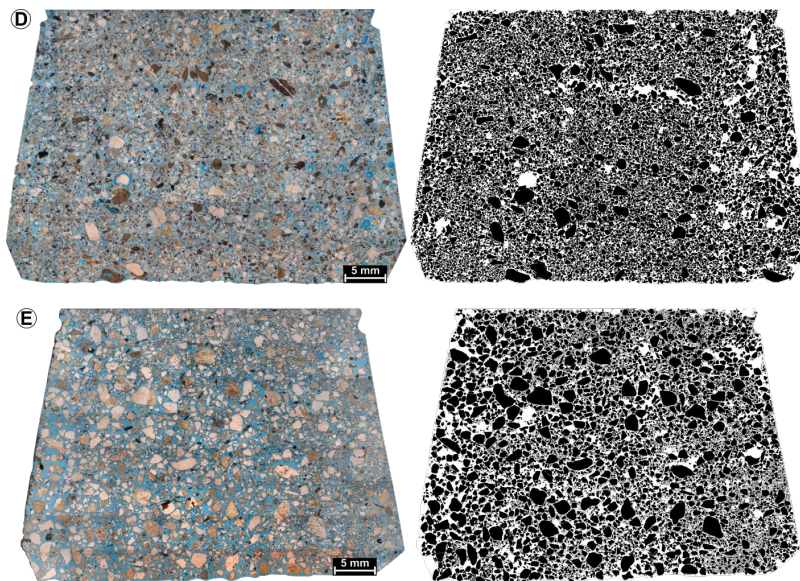
668 **Figure 11.** Original and binary photo-mosaics of the analyzed thin sections composed of tens of
669 photomicrographs stitched together. (a) LIM1 beach sample. (b) PAR1 fluvial sample. (c) PAR2 fluvial sample.
670 (d) PES1 fluvial sample. (e) ACQ1 fluvial-deltaic sample.

671

672 5.3.2 Basal fluvial sand bar sample (PAR1)



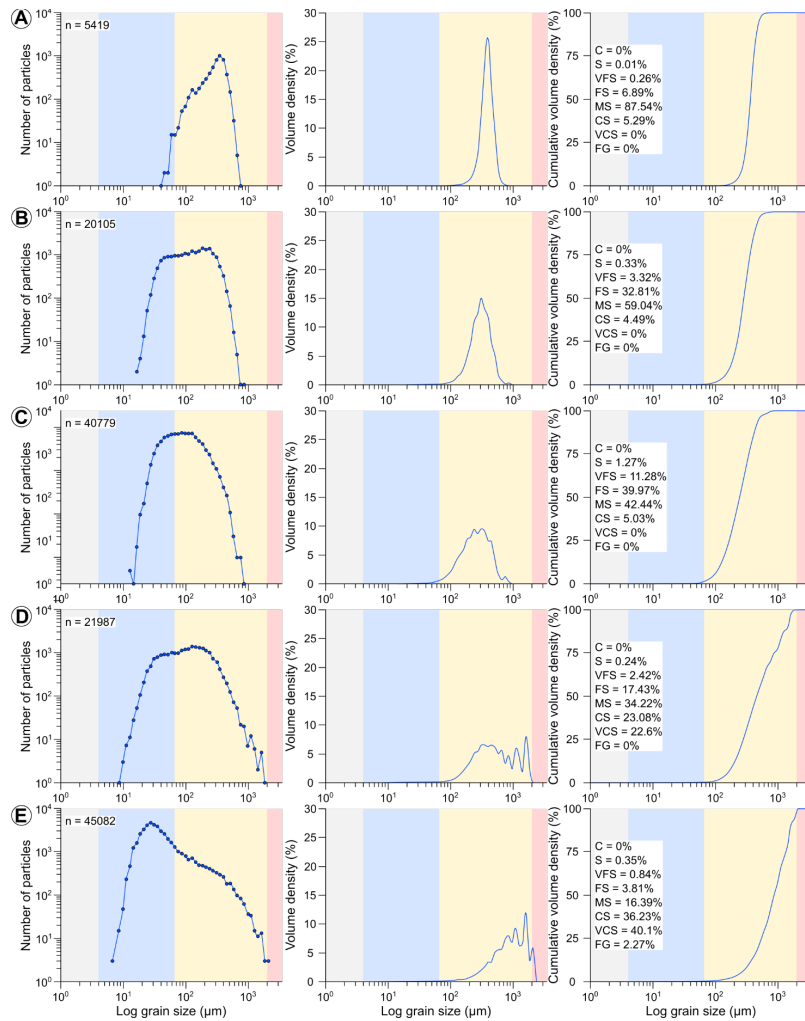
676 The fluvial sand bar sample PAR1 was analyzed by acquisition of 20,105 grains (Fig. 11b).
677 The particle number distribution describes a "bell-shape" curve, with the finest grains
678 recorded at 16.4 μm , coarsest ones at 859 μm and a mode of 186 μm . The density 679
volumetric distribution is described by a slight left asymmetry with a modal peak at 310 μm
680 (Fig. 12b). Sorting is lower compared to LIM1 sample, with a broader grain size distribution
681 as can be observed by particle volume density distribution through standard grain size 682
classes. The dominant size class is the medium-grained sand composing 59.04% of the
683 sample volume, followed by the fine-grained sand constituting 32.81% of volume density. 684
Lesser amounts of very fine-grained sand (3.32%) and coarse-grained sand (4.49%) have
685 been detected. Silt-sized material composes only 0.33% of the analyzed sample (Fig. 12b).



686
687 **Figure 11 continued.**

<https://doi.org/10.5194/egusphere-2023-2636>
Preprint. Discussion started: 15 November 2023
c Author(s) 2023. CC BY 4.0 License.





688

689 **Figure 12.** Grain size distribution curves extracted from 2D thin sections through image analysis. Results are
 690 presented as number of particles, volume density and cumulative volume percentage distributions. (a) LIM1
 691 beach sample. (b) PAR1 fluvial sample. (c) PAR2 fluvial sample. (d) PES1 fluvial sample. (e) ACQ1 fluvialdeltaic
 692 sample. n, number of particles. C, clay; S, silt; VFS, very fine-grained sand; FS, fine-grained sand; MS, medium-
 693 grained sand; CS, coarse-grained sand; VCS, very coarse-grained sand; FG, fine gravel.



694

695 *5.3.3 Upper fluvial sand bar sample (PAR2)*

696 40,779 grains were obtained from the second fluvial sand bar sample PAR2 (Fig. 11c). The
697 distribution of particle number is characterized by a symmetrical bell-shaped curve with finest
698 recorded particles at 12.7 μm , equivalent diameter of coarsest grains up to 859 μm and a
699 modal value of 86.4 μm . Although we defined one single modal value, the modal peak
700 described is wide and most of the grains have equivalent diameter falling between 58.9 and
701 127 μm . Data converted in particle volume density show a left asymmetry of the distribution
702 curve and a modal peak at 310 μm (Fig. 12c). The width of the curve (i.e., sorting degree) is
703 higher than the previous samples. Grains are almost equally distributed between the medium
704 and fine-grained sand size classes, with volume densities of 42.44% and 39.97%, respectively.
705 Significant particle volume is recorded in the very fine-grained sand size class (11.28%), while
706 only 5.03% of particles fall in the coarse-grained sand interval. Silt-sized material composes
707 1.27% of the total sample volume (Fig. 12c).

708 *5.3.4 Fluvially-reworked debris talus sand sample (PES1)*

709 PES1 sample, the reworked debris talus along the river stream, was analyzed by considering
710 a total of 21,987 grains (Fig. 11d). The distribution by number of particles describes a wide,
711 almost symmetrical bell-shape, having as lower and higher intercepts with X axis at 8.68 and
712 1,850 μm , respectively. The modal peak is broad, with most recurrent data in between 111 and
713 240 μm size interval and a modal value of 127 μm . The volume density corrected curve
714 displays a left asymmetry with a modal peak of 352 μm and a right curve tail with oscillating
715 volume density associated with coarser particles (Fig. 12d). The sorting degree is low as
716 indicated by the width of the modal peak. The volume density curve has a high width, testified
717 by the significant spread of particles in different grain size classes. In particular, the most
718 recurrent size class is the medium-grained sand interval with 34.22% of total grains, followed



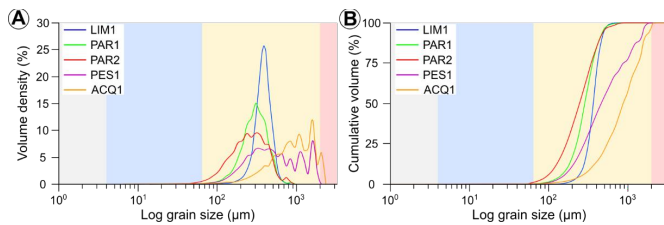
719 by the coarse-grained sand class composing 23.08% of the sample. Significant volume
720 densities of very coarse-grained and fine-grained sand are documented, with percentages of
721 22.6% and 17.43%, respectively. Small volume of very fine-grained sand material is recorded
722 (2.42%), together with silt-sized particles (0.24%) (Fig. 12d).

723 5.3.5 Deltaic sand sample (ACQ1)

724 Two-dimensional grain size of ACQ1 sample, collected along a fossil deltaic bar, was
725 investigated with a total amount of 45,082 grains (Fig. 11e). The number of grain distribution
726 highlights an asymmetric shape with right skew, and finest particles recorded at 6.72 μm and
727 coarsest ones at 2,100 μm . The modal value of the distribution lies in the fine-grained interval
728 at 27.4 μm . The volume density distribution curve displays a left asymmetry, with a gentle left
729 tail and a steep right tail showing marked data oscillations. The modal peak is located at 1,630
730 μm in the coarser end of the distribution curve and the sorting degree is low (Fig. 12e). In this
731 sample the dominant grain size fraction is the very coarse-grained sand with 40.1% of total
732 sample volume. Coarse and medium-grained sand classes compose 36.23% and 16.39% of
733 total sample volume, respectively. Minor amounts of fine-grained sand (3.81%) and fine gravel
734 (2.27%) are also documented. Finally, tiny fractions of very fine-grained sand and silt-size
735 material compose the fine tail of the curve with 0.84% and 0.35% of volume density,
736 respectively (Fig. 12e).

Deleted: Eventually

737 Summarizing the main results obtained from thin section analysis, we observe a progressive
738 broadening and coarsening of granulometric curves with different distribution of particles from
739 LIM1 to ACQ1 samples (Fig. 13a). In coarse-grained samples (PES1 and ACQ1) the coarse,
740 right tail of the distribution curves shows oscillating volume density values due to the presence
741 of a few tens of grains providing higher data scattering. The comparison of cumulative
742 frequency distribution confirms the diminishing of the slope due to lowering sorting degree (Fig.
743 13b).



745

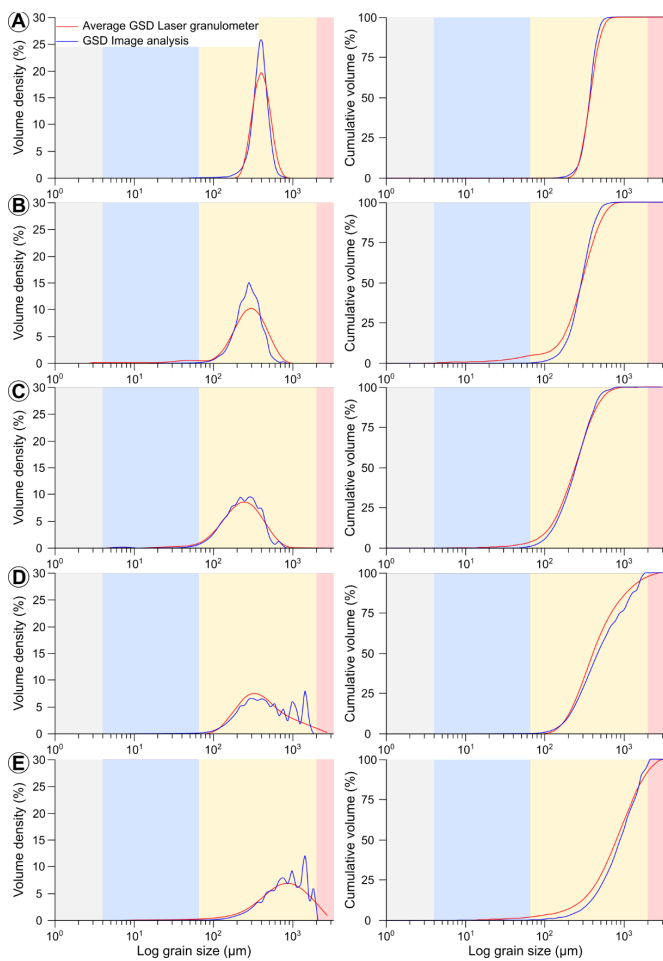
746 **Figure 13.** Comparison of grain size distributions obtained from image analysis technique applied to thin
747 sections. (a) Volume density grain size distributions. (b) Cumulative volume percentage grain size distributions.

748

749 **5.4 Laser granulometry vs. thin section grain size distributions**

750 The comparison between volume density distribution curves acquired via optical granulometry
751 and thin section analysis, shows striking similarities (Fig. 14). For all the 5 considered samples
752 both methods provide similar overall shape of grain size distributions with almost overlapping
753 modal peak values. Slight differences in modal peak height can be documented especially for
754 highly to moderately sorted samples (LIM1 and PAR1), in which the grain size distribution
755 curve obtained through image analysis has higher modal values compared to the laser
756 granulometer data (Fig. 14a and b). On the same samples, the laser granulometer technique
757 recorded higher particle volumes in the right (coarse) tail of granulometric curve with respect
758 to image analysis data. Tiny differences can be seen in the left (fine) tail of curves, with LIM1
759 displaying smaller particle volume recorded by laser granulometry with respect to thin sections,
760 while the opposite occurs for PAR1 sample. For the other 3 coarser and less sorted samples
761 (PAR2, PES1 and ACQ1) the match between the granulometric curves gained with different
762 methods is good and the intercepts with X axis are almost coincident (Fig. 14c-e).

Deleted: minor



764

765 **Figure 14.** Comparison between grain size distributions extracted from laser granulometry and from image
766 analysis. (a) LIM1 beach sample. (b) PAR1 fluvial sample. (c) PAR2 fluvial sample. (d) PES1 fluvial sample.
767 (e) ACQ1 fluvial-deltaic sample. GSD, grain size distribution. GSD, grain size distribution.

768



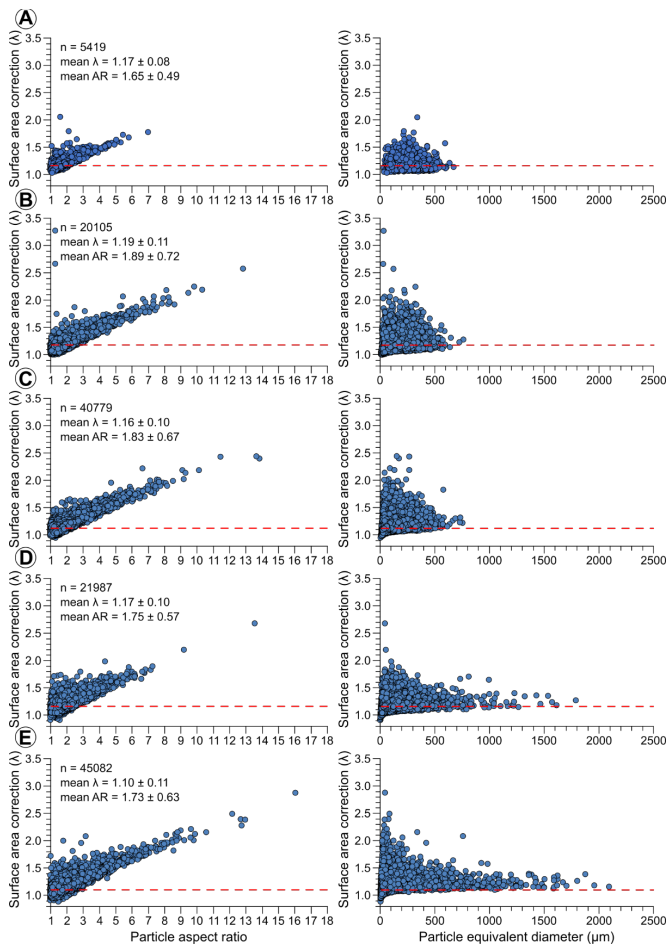
769 The main differences are related to the right (coarse) tail of the curves, especially for PES1
770 and ACQ1 samples, where the thin section distribution curve displays volume density
771 variability in the coarser grain size range. This data variability is induced by few very coarse
772 (1-2 mm size) particles, which influence the final volume density distribution (Fig. 14d and e).

773

774 **5.5 Volume-weighted mean diameter calculation**

775 Calculations of volume-weighted mean diameter were performed with the formula reported in
776 equation 2. The entire grain size datasets associated with thin sections of granular samples
777 were considered. The foreshore beach sand sample LIM1, returns a value of volume-weighted
778 mean diameter equal to 364.16 μm , while for the fluvial sand bar samples
779 (PAR1 and PAR2) mean values of 296.54 μm and 256.08 μm are obtained, respectively. PES1
780 fluvial coarse sand shows a volume-weighted mean diameter of 625.83 μm , and the fossil
781 deltaic sand ACQ1 sample provides a value of 955.79 μm . All the obtained mean diameter
782 values are lower than the equivalent obtained through optical laser granulometry.

783 We then applied a surface area correction factor (λ), as indicated in equation 3, to consider the
784 deviations of grain shape from spherical particles (Fig. 15) (Davies et al., 2019; Johnson et al.,
785 2021). λ factor was calculated for every sample and implemented in equation 2 as indicated in
786 the modified volume-weighted mean diameter formula reported in equation 4. For LIM1
787 sample, the aspect ratio of grains spans from 1.01 to 7.01, with a mean value of
788 1.65 ± 0.49 , thus equation 3 can be simplified and returns an average λ value of 1.17 ± 0.08
789 (Fig. 15a). By multiplying the volume-weighted mean diameter by λ factor, we obtain a
790 corrected grain diameter of 425.35 μm . PAR1 has grain aspect ratio falling between 1.01 and
791 12.84, with a mean value of 1.89 ± 0.72 , thus providing a mean λ correction factor of $1.19 \pm$
792 0.11 (Fig. 15b).



793

794 **Figure 15.** Graphs reporting the particle aspect ratio-surface area correction factor and particle equivalent
795 diameter-surface area correction factor relationships for the analyzed sand samples. **(a)** LIM1 beach sample.
796 **(b)** PAR1 fluvial sample. **(c)** PAR2 fluvial sample. **(d)** PES1 fluvial sample. **(e)** ACQ1 fluvial-deltaic sample.

797 The horizontal dashed red line indicates the average surface area correction factor. n, number of particles; λ ,
798 surface area correction factor; AR, particle aspect ratio.

799



800 The resulting corrected volume-weighted mean diameter is equal to 351.78 μm . For PAR2
801 sample, grains have aspect ratios ~~from 1.0 to 13.88~~ with an average value of 1.83
802 ± 0.67 , giving a mean λ value of 1.16 ± 0.1 (Fig. 15c). The volume-weighted mean diameter
803 corrected according to particle shape results 307.39 μm . PES1 is composed of grains with
804 aspect ratios ~~spanning from 1.0 to 13.55~~, with an average value of 1.75 ± 0.57 , returning a
805 mean λ correction factor of 1.17 ± 0.1 (Fig. 15d). Applying the correction to equation 4, the final
806 volume-weighted mean diameter is equal to 731.08 μm . ~~Finally, ACQ1 sample is characterized~~
807 by grains with aspect ratios ~~between 1.0 and 16.06~~ with an average value of
808 1.73 ± 0.63 , giving back a λ mean surface area correction factor of 1.10 ± 0.11 (Fig. 15e). The
809 obtained corrected equivalent diameter for this sample is 1,055.64 μm . Volumeweighted mean
810 diameter displays values close to the ones obtained through optical granulometry. The only
811 exception is PES1 sample, which has an average grain size measured with laser granulometry
812 90-100 μm finer than the values calculated via image analysis on thin section.

Deleted: comprised

Deleted: Eventually

813

814 6. Discussion

815 6.1 Comparison between 2D (image analysis) and 3D (laser granulometry) grain size 816 analyses

817 Grain size distribution curves of analyzed samples obtained from 2D (image analysis) and
818 3D (laser granulometry) methods show striking similarities. The overall shape, skew
819 (asymmetry) and modal peak position is equal in both the adopted methodologies (Fig. 14).
820 Slight differences can be traced in modal peak height, with data obtained through laser
821 granulometry displaying typically lower modal height with respect to grain size distributions
822 provided by image analysis from thin sections. Moreover, grain size distributions gained with
823 the optical granulometer appear to be smoother especially on the coarser tail compared to
824 image analysis data (Fig. 14). This can be explained by the usage of the 100 instrumental



827 grain size classes adopted by the laser granulometer, which were extended also to image
828 analysis grain size distributions. Such detailed subdivision of the 10 nm to 3,500 μm size
829 interval in tiny frequency bins, caused variations in the coarser end of grain size distributions
830 gained from image analysis. These variations are mainly related to the presence of a few tens
831 of grains in coarser grain size classes inducing volume frequency oscillations. We employed
832 the very same grain size classes for both analytical methods to allow precise comparison of
833 data distribution, without the bias induced by different bin sizes. It is likely that the adoption of
834 the standard sedimentological grain size classes (Udden-Wentworth scale) (Udden, 1914;
835 Wentworth, 1922) could have provided more stable volume frequency results at the cost of
836 less detail between different classes. Still, we preferred to prioritize and put emphasis on
837 evidencing small differences between grain size classes rather than achieving volume
838 frequency stability across the whole grain size distributions.

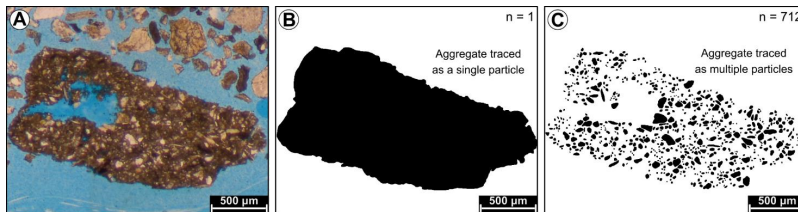
839 The comparison of volume-weighted mean diameters extracted from granulometry data, and
840 the corrected volume-weighted mean diameters from image analysis technique provided
841 matching results for 4 out of 5 total sand samples. In particular, for LIM1 sample, laser
842 granulometry returned a mean equivalent diameter of 434 μm , while image analysis technique
843 gave 425.3 μm . Fluvial sand PAR1 showed an equivalent diameter from laser granulometry of
844 352 μm , with related volume-weighted mean diameter of 351.8 μm , while for PAR2 returned
845 diameter values of 304 and 307.4 μm , respectively. In the case of PES1, the laser
846 granulometer measured a mean particle diameter of 639 μm , while data acquired with image
847 analysis provided a mean value of 731.1 μm . Finally, for the ACQ1 deltaic sand sample,
848 laboratory grain size analysis gave a mean diameter of 1,050 μm , while image analysis
849 technique provided a value of 1,055.6 μm . The only deviation from matching results was
850 related to PES1 sample, which showed image analysis derived data 90-100 μm coarser than
851 the equivalent diameter measured via laser granulometry. We explain this difference
852 considering the mineralogical composition of the sample and the limits imposed by the involved

Deleted: Eventually

Deleted: good and



855 analytical techniques. Apart from quartz, feldspar, and plagioclase, PES1 sample is composed
856 of coarse aggregates of silt-clay matrix binding fine-grained siliciclastic grains (Fig. 16a).
857 During manual tracing of particle outer boundaries, we treated these aggregates as single
858 particles, without distinguishing the fine-grained particles interspersed within the matrix (Fig.
859 16b and c).



860
861 **Figure 16.** Soft aggregates issue encountered in manual digitization of PES1 sample. (a) Soft, ~2 mm-size,
862 aggregate composed of clayish matrix embedding fine-grained siliciclastic particles. (b) Digitization strategy
863 adopted in the present study for such clay aggregates. (c) Digitization of every particle composing the interior
864 of the aggregate. n, number of traced grains.

865 Thin sectioning of loose granular media, proved to be a conservative method in preserving the
866 original size and shape of weak sand framework components, minimizing the overall sample
867 alteration. Conversely, laser granulometry operated via pressured air dispersion may cause
868 alteration of original grain size in sensitive and mechanically weak samples (Storti and
869 Balsamo, 2010; Cortinovis et al., 2019). Before the analyses we performed tests to set the
870 instrumental parameters to be used giving the least sample alteration (Supplementary material
871 1). In the case of PES1, which is the weakest sample, even the adoption of the most
872 conservative analytical parameters was not enough to completely avoid sample damage. This
873 sample is the only one displaying aggregates whose matrix is made of clay minerals, which
874 could have been damaged during laser granulometry analysis. In PES1 some alteration,
875 related to splitting and partial disaggregation of soft silt-clay aggregates caused the fine-ward
876 shift of the average particle diameter. In such weak sample types, we considered data derived

Deleted: granting

Deleted: ing



879 from image analysis technique to be more reliable and representative of the real grain size
880 distribution than laser granulometry analysis. The same alteration was not documented in the
881 other 4 samples likely due to their different mineral composition and higher relative particle
882 resistance, preventing any significant mechanical alteration of the original grain size during the
883 analysis.

884

885 **6.2 Volume-weighted mean diameter (D_w) vs. literature calculation methods**

886 Mean particle diameter values based on optical granulometry and image analysis (corrected
887 volume-weighted mean diameter) methods were compared with previously published and
888 widely used calculation equations reported in the Appendix 1 (tables 2 and 3). In particular, we
889 focused on the comparison with the method of moments (both arithmetic and geometric
890 equation) (Krumbein and Pettijohn, 1938), the graphical method (geometric mean) (Folk and
891 Ward, 1957), median, mode, arithmetic mean and area-weighted mean diameter. In comparing
892 different equations, we assumed the mean diameter values extracted from the laser
893 granulometer as reference, with relative differences between calculation formulas expressed
894 as percentages (positive values represent grain diameter underestimation, while negative
895 ones indicate overestimation with respect to the reference) (tables 2 and 3). Considering laser
896 granulometry reference data, the arithmetic mean calculated with the method of moments,
897 provides close results with the ones gained with the mean diameter formula employed by the
898 optical granulometer (equation 5) (maximum difference in the average grain diameter of 0.36%
899 from the reference value). Conversely, the geometrical mean of method of moments returns
900 small percentage errors for well sorted samples (3.1% difference for LIM1 sample) with a
901 progressively increasing error following sorting diminishing (from 16.4 to 24.4% error in PAR1,
902 PAR2, PES1 and ACQ1 samples) (table 2).

903

Table 2: Comparison of results from different calculation equations applied to laser granulometry analyses



Sample name	Method of moments		Graphical method	GSD laser granulometry			
	Arithmetic (μm)	Geometric (μm)	Geometric (μm)	Sorting	D_m (μm)	Median (μm)	Mode (μm)
LIM1	434.7	420.5	420.6	0.37	434	420	419
PAR1	352.9	294.3	319.8	0.845	352	328	350
PAR2	305.1	252.7	261.1	0.877	304	267	286
PES1	640.3	492.6	487.5	1.029	639	455	386
ACQ1	1053.6	794.1	850.7	1.137	1050	897	1020

Sample name	Complementary percentage ratio with respect to volume-weighted mean diameter from laser granulometry (%)						
LIM1	-0.16	3.11	3.09	-	0	3.22	3.45
PAR1	-0.25	16.39	9.15	-	0	6.82	0.57
PAR2	-0.36	16.87	14.11	-	0	12.17	5.92
PES1	-0.20	22.91	23.71	-	0	28.79	39.59
ACQ1	-0.34	24.37	18.98	-	0	14.57	2.86

904

905 **Table 2.** Comparison of results given by different calculation formulas for grain size distribution acquired through
 906 laser granulometry. Calculation equations are reported in the Appendix 1. GSD, grain size distribution; D_m ,
 907 average grain diameter (laser granulometer).

908 The same increasing error trend can be seen for the geometric mean of graphical method, with
 909 a maximum deviation of 23.7% calculated for PES1 sample. Finally, the median of distribution
 910 curves is close to the mean diameter gained from laser granulometry only in the case of well
 911 sorted samples (deviation of 3.2 and 6.8% in LIM1 and PAR1, respectively), while it deviates
 912 far from it in more poorly sorted ones (PAR2, PES1 and ACQ1, with errors up to 28.8%). The
 913 mode can approximate the average diameter only in the case of weakly skewed grain size
 914 distributions (errors comprised from 0.5 to 5.9% in LIM1, PAR1, PAR2 and ACQ1), but it fails
 915 in the case of strongly skewed ones (39.6% deviation in PES1) (table
 916 2).

917 Utilizing grain size distribution datasets extracted via image analysis, (the corrected volume-
 918 weighted mean diameter is used as reference) the best results are provided by applying the
 919 arithmetic method of moments, with standard errors from 1.7 to 3.9% in all samples. As already
 920 observed for laser granulometer size distributions, geometrical mean calculated with the
 921 method of moments returns good results only for well sorted samples, and tends to

Deleted: Eventually

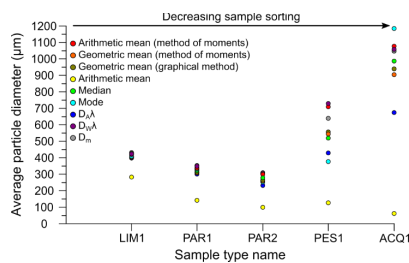
Deleted: technique

Deleted: spanning

Deleted: while



926 underestimate the mean diameter up to 25.3% of reference value in poorly sorted sands (Fig.
 927 17 and table 3).



928
 929 **Figure 17.** Comparison of average particle diameter values calculated with literature equations and the proposed
 930 volume-weighted mean diameter formula for the 5 samples. Used datasets are derived from thin sections
 931 analyzed with image analysis. $D_A \lambda$, area-weighted mean diameter (shape corrected); $D_w \lambda$, volume-weighted
 932 mean diameter (shape corrected). D_m , laser granulometer mean diameter. Similar results are extracted
 933 from the geometric mean diameter formula of the graphical method, with the best result
 934 achieved for LIM1 sample (4.2% mean diameter underestimation) and worst attained for PES1
 935 sand sample (23.7% diameter underestimation). Adoption of the median value gives good
 936 results for properly sorted samples (-0.4 to 7.7% in LIM1 and PAR1), while deviations become
 937 bigger in poorly sorted ones (10.9 and 28.9% in PAR2 and PES1, respectively) (Fig. 17). The
 938 mode follows similar trends and fails in describing weakly to poorly sorted granular media
 939 (errors from -12.2 to
 940 48.6% in PAR2, PES1 and ACQ1). Severe mean diameter underestimation is documented
 941 in the case of simple arithmetic mean diameter and area-weighted mean diameter with
 942 standard errors reaching 94.1 and 41.3%, respectively (Fig. 17 and table 3).

Deleted: considered sand

Deleted: grants

943 Table 3: Comparison of results from different calculation equations applied to image analysis grain size data

Sample name	Method of moments		Graphical method		GSD Image analysis				
	Arithmetic (μm)	Geometric (μm)	Geometric (μm)	Sorting	Arithmetic (μm)	Median (μm)	Mode (μm)	$D_A \lambda$ (μm)	$D_w \lambda$ (μm)
LIM1	415.4	403.2	407.5	0.329	283.8	427	411.2	401.4	425.3
PAR1	337.8	313.5	317.7	0.544	141.4	324.5	331	300	351.8
PAR2	302	264.6	267.2	0.757	98.63	273.9	256	232.7	307.4



PES1	709.6	546.3	557.4	1.097	127.8	519.6	376	428.9	731.1
ACQ1	1079.1	906.5	940.5	0.901	62.4	989.1	1185	674.6	1055.6
Sample name	Complementary percentage ratio with respect to volume-weighted mean diameter from image analysis (%)								
LIM1	2.33	5.19	4.18	-	33.27	-0.4	3.31	5.62	0
PAR1	3.98	10.88	9.69	-	59.81	7.76	5.91	14.72	0
PAR2	1.75	13.92	13.08	-	67.91	10.89	16.72	24.30	0
PES1	2.94	25.27	23.76	-	82.52	28.93	48.57	41.33	0
ACQ1	-2.22	14.12	10.90	-	94.09	6.29	-12.26	36.09	0

946

947

948

949

950

951

952

953

954

955

956

957

958

959

960

961

Table 3. Comparison of results provided by different calculation formulas for grain size distributions gained with image analysis. Calculation equations are reported in the Appendix 1. GSD, grain size distribution; D_{λ} , area-weighted mean diameter (shape corrected); $D_{w\lambda}$, volume-weighted mean diameter (shape corrected). Summarizing the comparative results, the proposed corrected volume-weighted mean diameter equation proves to be a reliable calculation formula and provides matching results with the arithmetic method of moments, as well as with data gained from laser granulometry technique. Conversely, the geometrical mean diameter of both method of moments and graphical method can describe only well to moderately sorted samples, while it struggles in poorly sorted ones. The same deviations, with even bigger magnitudes, can be highlighted by the adoption of the median and modal value as parameters describing grain size distributions. Similarly, the simple arithmetic mean, and area-weighted mean diameter are not reliable calculation equations, and their usage should be avoided as they show the highest difference from the reference (tables 2 and 3).

6.3 Shape correction factor (λ) vs. literature empirical correction parameters

962

963

964

965

966

In the past years, many efforts were made to achieve robust conversion factors that could give reliable 3D average particle diameter starting from 2D equivalent diameter distributions obtained with different analytical methods. Correction equations have been developed in different research areas of Earth Sciences, from sedimentology, planetary geology, to structural geology. Correction coefficients are based on geometrical considerations

Deleted: a lot of

Deleted: grant

Deleted: spanning



970 (Roethlisberger, 1955; Hughes, 1978b), statistical-mathematical relationships (Krumbein,
971 1935; Chayes, 1950; Greenman, 1951; Sahu, 1966; Rose, 1968; Johnson, 1994; Kong et al.,
972 2005), empirical rules (Friedman, 1962a) or software aided simulations (Panozzo Heilbronner,
973 1992; Heilbronner and Bruhn, 1998). All these methods bring different correction coefficients
974 to account for mean diameter underestimation related to random particle sectioning.
975 Correction values are between 1.0 and 1.5 and must be multiplied by the average grain
976 diameter obtained from image analysis performed on rock thin sections (table 4). We tested
977 the precision of equations proposed in literature by applying the correction coefficient to the
978 volume-weighted mean diameter values obtained from the 5 studied sand samples. In this
979 process, we did not multiply the mean diameter by the λ shape correction factor, thus using
980 only the raw, uncorrected volume-weighted mean diameter values (table 4). Such a procedure
981 allowed a direct comparison of λ shape correction factor with other correction parameters. By
982 using our grain size datasets, closest results compared to the ones obtained with equation 4,
983 are gained employing the correction factors proposed by Friedman (1958, 1962b), Sahu
984 (1966), and Johnson (1994). Other correction methods (Krumbein, 1935; Chayes, 1950;
985 Greenman, 1951; Hughes, 1978b; Panozzo, 1982; Panozzo Heilbronner, 1992; Kong et al.,
986 2005) typically tend to overestimate the average grain diameter by a significant margin (table
987 4). This is especially true in the case of poorly sorted, coarse-grained samples (PES1 and
988 ACQ1), while differences are less pronounced in well to moderately sorted and medium-
989 grained ones (LIM1 and PAR1) (table
990 4). Although some of the correction methods discussed above provide close results with the
991 shape corrected volume-weighted mean diameter values, we prefer to apply different λ
992 correction factors to different samples. This sample specific procedure should give more
993 reliable results, due to shape correction bound to the grain size distribution and particle form
994 of each sample.

Deleted: comprised

Deleted: grant

995 Table 4: Comparison of correction parameters with the presented original data



Literature correction method	Mean diameter of analyzed samples (μm)					Correction factor
	LIM1	PAR1	PAR2	PES1	ACQ1	
Krumbein (1935), Chayes (1950), Kong et al. (2005)	463.65	447.88	337.5	796.81	1216.91	1.2732
Krumbein (1935)	477.27	388.64	335.62	820.21	1252.65	1.3106
Greenman (1951)	494.86	402.39	348.03	851.04	1299.63	1.3589
Friedman (1958), (1962)	430.18	350.30	363.12	739.29	1129.07	1.1813
Sahu (1966)	412.15	335.62	289.83	708.31	1081.76	1.1318
Hughes (1978)	445.98	363.17	313.62	766.45	1170.55	1.2247
Panozzo (1982)	466.12	379.57	327.78	801.06	1223.41	1.28
Heilbronner (1992)	546.24	444.81	384.12	938.74	1433.68	1.5
Johnson (1994)	418.79	340.56	294.53	720.26	1099.92	1.15
D_v λ image analysis	425.35	351.78	307.39	731.08	1055.64	1.10-1.19
D_w uncorrected image analysis	364.16	296.54	256.08	625.83	955.79	
D_m laser granulometry	434	352	304	639	1050	

998

999

1000

1001

Table 4. Comparison of different published correction factors to be applied in switching from 2D to 3D grain size distributions. D_m , mean grain diameter (laser granulometer); D_w , volume-weighted mean diameter; λ , shape correction factor.

1002

1003

6.4 Representative number of particles-sorting relationship

1004

In all the analyzed samples, we acquired large particle size datasets (> 5,000 particles), as we were interested in testing the reliability and reproducibility of mean diameter calculated with the proposed volume-weighted mean diameter formula. The number of digitized particles was higher in samples characterized by low sorting degree, and this was required to extract stable mean diameter values. At the same time, the adoption of large datasets allowed to check the critical number of particles required to achieve a certain standard error

1005

1006

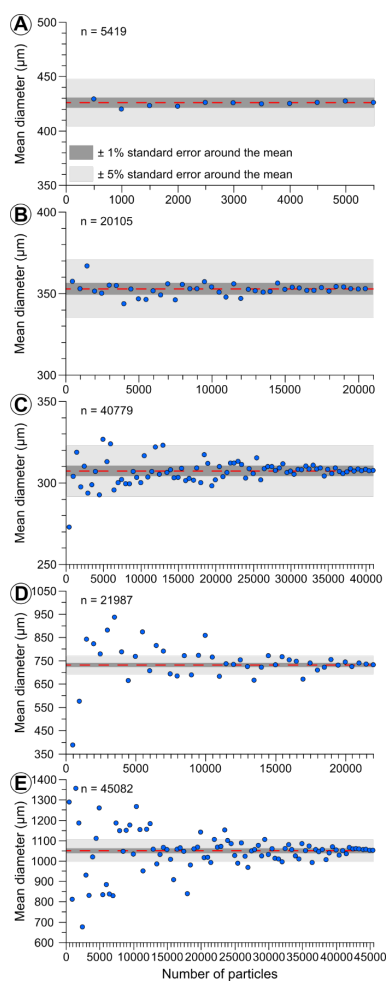
1007

1008

1009



992 associated with the mean diameter, using as reference the volume-weighted mean diameter 993 calculated with all available particles.



994



995

Figure 18. Volume-weighted mean diameter vs number of particles relationship calculated for 500 grains 996 incremental bins. Standard error (± 1 and 5%) intervals are calculated with respect to the average diameter

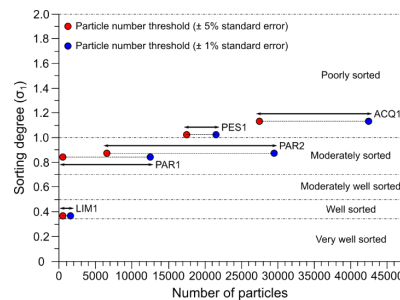


997 obtained from the entire grain size datasets (red dashed line). (a) LIM1 beach sample. (b) PAR1 fluvial sample.
998 (c) PAR2 fluvial sample. (d) PES1 fluvial sample. (e) ACQ1 fluvial-deltaic sample. n, number of particles.

999 To do so, we calculated the volume-weighted mean diameter at incremental steps of 500
1000 particles and we checked the deviation with respect to the reference value. At every calculation
1001 step, particles were randomized using a modified shuffle Matlab[®] algorithm to avoid any bias
1002 in particle extraction. We assumed two different confidence levels compiled at $\pm 1\%$ and $\pm 5\%$
1003 standard error of the average diameter obtained with all available particles (Fig. 18). For LIM1
1004 beach sand sample, volume-weighted mean diameter lays just outside the $\pm 1\%$ standard
1005 error interval, using only 500-1,000 particles, while it becomes more stable and between $\pm 1\%$
1006 standard error for datasets $> 1,500$ grains (Fig. 18a). For this sample the minimum particle
1007 number is low due to the good sorting degree. PAR1 fluvial sand sample displays average
1008 diameter values always between the $\pm 5\%$ error interval (already for 500 grains), but only using
1009 12,500 particles or more, the calculated values fall in the $\pm 1\%$ standard error (Fig. 18b). PAR2
1010 sample shows a more marked scattering of data for limited particle number ($< 5,000$ grains),
1011 while the critical $\pm 5\%$ error threshold is attained at 6,500 grains and the more restrictive $\pm 1\%$
1012 standard error is achieved for 29,500 particles (Fig. 18c). Mean diameter values for PES1
1013 sample are characterized by strong variations up to 5,000-7,000 used grains, while they
1014 become more stable above 10,000 particles, reaching the $\pm 5\%$ standard error threshold at
1015 17,500 particle and the $\pm 1\%$ error at 21,500 grains, respectively (Fig. 18d). Eventually, the
1016 poorly sorted ACQ1 sample displays volumeweighted mean diameter values outside the $\pm 5\%$
1017 error interval up to 10,000-15,000 grains. At least 27,500 particles are needed to calculate
1018 average diameter values in the $\pm 5\%$ standard error interval and 42,500 grains must be used
1019 to achieve the $\pm 1\%$ threshold (Fig. 18e). A decrease of sorting degree (widening of
1020 granulometric curves) from 0.37 to 1.137 causes an increase in the minimum number of
1021 particles to be used in average diameter calculation from 500 to 27,500 to reach the $\pm 5\%$
1022 standard error threshold (Fig. 19). To attain the $\pm 1\%$ error interval on the same samples, 1,500



1023 to 42,500 particles are required (Fig. 19). We tested the importance of the number of particles
1024 used in sample with relatively simple size distribution curves (single mode and gentle curve
1025 asymmetry).



1026

1027 **Figure 19.** Critical particle number vs sorting degree relationship calculated for the 5 analyzed samples based
1028 on volume-weighted mean diameter calculations.

1029 It is likely that samples with poorer sorting, multi-mode distributions and stronger asymmetry
1030 could require even larger particle amounts (Friedman, 1962a; Heilbronner and Barrett, 2014;
1031 Lopez-Sanchez, 2020). This aspect should be carefully considered when extracting average
1032 particle diameter from small datasets and results should be treated cautiously, being aware of
1033 the low reliability induced by limited data.

1034

1035 6.5 Fields of application and usefulness of the proposed method

1036 Volume-weighted mean diameter proved to be a reliable parameter to describe 3D grain size
1037 distribution from 2D grain size datasets acquired through image analysis applied on thin
1038 sections. The addition of sample-specific λ shape correction factors facilitates the conversion
1039 from 2D to 3D grain size distributions. Moreover, the calculation formula is straightforward and
1040 can be easily used, without requiring specific stereologicalmathematical knowledge (Elias,
1041 1967; Underwood, 1970; Russ, 1986; Gallagher et al., 2023). Our tests have been performed



1042 on loose sand samples, but the volume-weighted mean diameter could be particularly useful
1043 in the case of cohesive and hardened granular media not suitable to be analyzed through
1044 other laboratory techniques (optical granulometry, electro-resistivity methods, pipette, or
1045 sedimentation). Grain size analysis on such sample types must be conducted by means of
1046 microscopy characterization in conjunction with image analysis (Krumbein, 1935). Basic
1047 image analysis software, such as ImageJ, provides every required factor to be inserted in the
1048 calculation equation (Schneider et al., 2012). We preferred to manually digitize all the 2D grain
1049 size datasets employed to set the mean diameter formula, to achieve the maximum precision
1050 in defining particle shape and outer boundaries. However, as this procedure is extremely time
1051 consuming (7-10 days of work for each thin section image), it may be seen as poorly viable
1052 and suitable in the case numerous samples to be analyzed (Heilbronner and Barrett, 2014).
1053 In the past years, many efforts have been made to process large number of images both with
1054 semi-automatic and automatic methods (Mazzullo and Kennedy, 1985; Eicken, 1993;
1055 Heilbronner and Bruhn, 1998; Ketcham, 2005; Mock and Jerram, 2005; Gualda, 2006; Berger
1056 et al., 2011; LopezSanchez and Llana-Fúnez, 2016). Image segmentation has become a more
1057 reliable, efficient and easy procedure, leading to the acquisition of thousands of grain size data
1058 in few hours of processing with acceptable errors (Heilbronner and Barrett, 2014). In recent
1059 years, some authors developed image segmentation algorithms which employ computer
1060 artificial intelligence and machine learning processes in particle segmentation, further
1061 reducing data acquisition time (Saxena et al., 2021). By taking advantage of these recent
1062 techniques, users should not be concerned about the minimum number of representative
1063 particles to be used in calculating volume-weighted mean diameter, even at the highest
1064 desired precision intervals. Following this, we encourage scientists of different research areas,
1065 to experiment and test the usefulness of the proposed corrected volume-weighted mean
1066 diameter as it provided precise and reliable results in samples with different textural
1067 characteristics, grain size distributions and mineral compositions.

Deleted: technique



1069

1070 7. Concluding remarks

1071 The correct measuring of particle size distributions and particle-grain mean diameters is
1072 fundamental in the study and characterization of both natural and artificial granular media.
1073 Several analytical procedures and calculation equations have been set up in the last decades.
1074 However, the comparison between 2D and 3D datasets acquired with different techniques is
1075 not straightforward. To address this issue, we proposed the use of volume-weighted mean
1076 diameter, an easy-to-use equation designed to define 3D equivalent particle diameter from 2D
1077 datasets gained through image analysis technique. The corrected volume-weighted mean
1078 diameter equation that has been set is capable of accurately describing grain size distribution
1079 on different sample types. Apart for the volume-weighing, the equation takes also into account
1080 particle shapes and is suitable for granular samples with different textural characteristics and
1081 mineral compositions. The following conclusive points can be drawn from our study:

1082 1- Volume-weighted mean diameter provides matching results with particle size data
1083 gained through optical granulometry technique, and combined with thin sectioning, can
1084 be useful in the case of weak or sensitive samples that can be partially compromised
1085 by laser diffraction or other analytical methodologies. In such sample types, 2D image
1086 analysis gives much more conservative and representative results than laser
1087 granulometry.

1088 2- Employing both laser granulometry and image analysis datasets, volume-weighted
1089 mean diameter returns close results compared to the methods of moments (arithmetic
1090 mean) equation. Conversely, other calculation formulas (geometric mean of method of
1091 moments, geometric mean of graphical method, median, and mode) proved to be less
1092 reliable and more sample sensitive (goodness of results may vary according to sample
1093 sorting and skewness).

Deleted: help

Deleted: ing

Deleted: grants



1097 3- The calculation of accurate and precise average diameter values requires an
1098 increasing particle number following the diminishing of sorting degree (widening of
1099 grain size distribution). However, automatic to semi-automatic particle identification and
1100 image analysis processing could help in reducing the time required for the acquisition
1101 of such large particle datasets.

1102 4- The adoption of volume-weighted mean diameter provides reliable data and allows the
1103 estimation of 3D average diameter from 2D particle datasets. This process is based on
1104 a relatively simple equation, employing basic input parameters, without recurring to
1105 advanced stereology concepts or difficult mathematical equations.

1106 Given the summary points described above, we suggest researchers working on different
1107 disciplines dealing with particle size determination to test the volume-weighted mean diameter
1108 equation and check whether it could be a viable solution for straightforward mean diameter
1109 calculation from 2D data distributions.

1110

1111 **Declaration of competing interests**

1112 The authors declare that they have no known competing financial interests or personal
1113 relationships that could have appeared to influence the work reported in this paper.

1114

1115 **Author contributions**

1116 Mattia Pizzati: Conceptualization, Supervision, Data curation, Formal analysis, Methodology,
1117 Writing original draft, Writing - review & editing, Validation.

1118 Luciana Mantovani: Conceptualization, Data curation, Formal analysis, Methodology, Writing
1119 - review & editing.



1120 Antonio Lisotti: Conceptualization, Data curation, Methodology.

1121 Fabrizio Storti: Conceptualization, Supervision, Writing - review & editing.

1122 Fabrizio Balsamo: Conceptualization, Supervision, Writing - review & editing, Validation,

1123 Funding acquisition.

1124

1125 **Acknowledgements**

1126 This work has benefited from the equipment and framework of the COMP-HUB and COMP-
1127 R Initiatives, funded by the 'Departments of Excellence' program of the Italian Ministry for
1128 University and Research (MIUR, 2018-2022 and MUR, 2023-2027). This work was supported
1129 by the research project '*Earthquake cycle in shallow sediments*' (FIL Quota
1130 Incentivante, Bando competitivo di Ateneo per la Ricerca 2020, Azione 1) granted to Fabrizio
1131 Balsamo, funded by University of Parma and Cariparma. Andrea Comelli (University of Parma)
1132 is kindly acknowledged for thin section preparation.

1133

1134 **Supplementary material**

1135 Details regarding the standard operating procedures adopted in optical granulometry
1136 analyses, XRD patterns, and high-resolution thin section photomosaics shown in Fig. 11 are
1137 reported in the online Supplementary material.

1138

1139 **Appendix 1**

1140 Hereafter are listed and explained the equations of the calculation formulas used in comparing
1141 particle diameter values in tables 2 and 3. We adopted the equations implemented in



1142 GRADISTAT, grain size statistical analysis software (Blott and Pye, 2001). Arithmetic and
1143 geometric means from the method of moments have been used (Krumbein and Pettijohn,
1144 1938), and the first one is defined as:

$$1145 \bar{x}_a = \frac{\sum_{i=0}^{i=n} f m_m}{100} \quad (A1)$$

1146 where, \bar{x}_a is the arithmetic mean, $f m_m$ stands for the frequency percentage of particles at the
1147 midpoint (m) of each size class (i).

1148 Conversely, the geometric mean of the method of moments is given by the equation:

$$1149 \bar{x}_g = \frac{\sum_{i=0}^{i=n} f \ln m_m}{100} \quad (A2)$$

1150 where, \bar{x}_g is the geometric mean, $f \ln m_m$ is the logarithmic frequency of particles at the midpoint
1151 (m) of each size class (i).

1152 The graphical method has been employed as well, with the geometrical mean and sorting
1153 degree (Folk and Ward, 1957; Folk, 1974). The geometrical mean diameter is described by
1154 the equation:

$$1155 M_G = \exp \frac{\ln P_{16} + \ln P_{50} + \ln P_{84}}{3} \quad (A3)$$

1158 where, M_G is the geometrical mean and P_{16} , P_{50} and P_{84} are the particle diameter values in
1159 metric units at the 16, 50 and 84% cumulative percentile of the particle size distribution curve,
1160 respectively.

1161 Sorting degree (σ_1) is provided by the standard deviation associated with the logarithmic mean
1162 (Folk, 1974) and is given by the equation:

$$1163 \sigma_1 = \frac{\Phi_{84} - \Phi_{16}}{4} + \frac{\Phi_{95} - \Phi_5}{6.6} \quad (A4)$$



1164 in which, Φ is the grain diameter in phi units, at 5, 16, 84 and 95% cumulative percentile values
1165 of the particle size distribution curve, respectively.

1166

1167 **References**

- 1168 Adams, J.: Sieve size statistics from grain measurement, *J. Geol.*, 85, 209–227, 1977.
- 1169 Agrawal, Y. C., McCave, I. N., and Riley, J. B.: Laser diffraction size analysis, in: Syvitski,
1170 J.M.P. (eds.) *Principles, methods and application of particle size analysis.*, Cambridge
1171 University Press, Cambridge, UK., 119–128, 1991.
- 1172 Bah, A. R., Kravchuk, O., and Kirchhof, G.: Fitting Performance of Particle-size Distribution
1173 Models on Data Derived by Conventional and Laser Diffraction Techniques, *Soil Sci. Soc.
1174 Am. J.*, 73, 1101–1107, <https://doi.org/10.2136/sssaj2007.0433>, 2009.
- 1175 Balsamo, F. and Storti, F.: Size dependent comminution, tectonic mixing and sealing
1176 behavior of a “structurally oversimplified” fault zone in poorly lithified sands: Evidence for a
1177 coseismic rupture?, *Bull. Geol. Soc. Am.*, 123, 651–668, <https://doi.org/10.1130/B30099.1>,
1178 2011.
- 1179 Balsamo, F., Storti, F., Salvini, F., Silva, A. T., and Lima, C. C.: Structural and petrophysical
1180 evolution of extensional fault zones in low-porosity, poorly lithified sandstones of the
1181 Barreiras Formation, NE Brazil, *J. Struct. Geol.*, 32, 1806–1826,
1182 <https://doi.org/10.1016/j.jsg.2009.10.010>, 2010.
- 1183 Balsamo, F., Storti, F., and Gröcke, D.: Fault-related fluid flow history in shallow marine
1184 sediments from carbonate concretions, Croton basin, south Italy, *J. Geol. Soc. London*,
1185 169, 613–626, <https://doi.org/10.1144/0016-76492011-109>.Fault-related, 2012.
- 1186 Barrett, P. J.: The shape of rock particles, a critical review, *Sedimentology*, 27, 291–303, 1980.
- 1187 Basumallick, S.: A note on thin section mechanical analysis, *J. Sediment. Res.*, 34, 194– 195,
1188 <https://doi.org/10.1306/74d7100f-2b21-11d7-8648000102c1865d>, 1964.
- 1189 Bense, V. F., Gleeson, T., Loveless, S. E., Bour, O., and Scibek, J.: Fault zone
1190 hydrogeology, *Earth-Science Rev.*, 127, 171–192,
1191 <https://doi.org/10.1016/j.earscirev.2013.09.008>, 2013.
- 1192 van den Berg, E. H., Bense, V. F., and Schlager, W.: Assessing textural variation in laminated
1193 sands using digital image analysis of thin sections, *J. Sediment. Res.*, 73, 133– 143,
1194 <https://doi.org/10.1306/061502730133>, 2003.
- 1195 Berger, A., Herwegh, M., Schwarz, J. O., and Putlitz, B.: Quantitative analysis of crystal/grain
1196 sizes and their distributions in 2D and 3D, *J. Struct. Geol.*, 33, 1751–1763,
1197 <https://doi.org/10.1016/j.jsg.2011.07.002>, 2011.
- 1198 Beuselinck, L., Govers, G., Poesen, J., Degraer, G., and Froyen, L.: Grain-size analysis by
1199 laser diffractometry: comparison with the sieve-pipette method, *Catena*, 32, 193–208,
1200 [https://doi.org/10.1016/S0341-8162\(98\)00051-4](https://doi.org/10.1016/S0341-8162(98)00051-4), 1998.



- 1201 Bianchi, G. G., Hall, I. R., McCave, I. N., and Joseph, L.: Measurement of the sortable silt
1202 current speed proxy using the Sedigraph 5100 and Coulter Multisizer Iie: Precision and
1203 accuracy, *Sedimentology*, 46, 1001–1014, <https://doi.org/10.1046/j.13653091.1999.00256.x>,
1204 1999.
- 1205 Billi, A.: Grain size distribution and thickness of breccia and gouge zones from thin (<1 m)
1206 strike-slip fault cores in limestone, *J. Struct. Geol.*, 27, 1823–1837,
1207 <https://doi.org/10.1016/j.jsg.2005.05.013>, 2005.
- 1208 Bittelli, M., Andrenelli, M. C., Simonetti, G., Pellegrini, S., Artioli, G., Piccoli, I., and Morari, F.:
1209 Shall we abandon sedimentation methods for particle size analysis in soils?, *Soil Tillage
1210 Res.*, 185, 36–46, <https://doi.org/10.1016/j.still.2018.08.018>, 2019.
- 1211 Blenkinsop, T. G.: Cataclasis and Processes of Particle Size Reduction, *Pageoph*, 136, 59–
1212 86, 1991.
- 1213 Blott, S. J. and Pye, K.: Gradistat: A grain size distribution and statistics package for the
1214 analysis of unconsolidated sediments, *Earth Surf. Process. Landforms*, 26, 1237–1248,
1215 <https://doi.org/10.1002/esp.261>, 2001.
- 1216 Blott, S. J. and Pye, K.: Particle size distribution analysis of sand-sized particles by laser
1217 diffraction: An experimental investigation of instrument sensitivity and the effects of particle
1218 shape, *Sedimentology*, 53, 671–685, <https://doi.org/10.1111/j.1365-3091.2006.00786.x>,
1219 2006.
- 1220 Blott, S. J., Croft, D. J., Pye, K., Saye, S. E., and Wilson, H. E.: Particle size analysis by
1221 laser diffraction, *Geol. Soc. Spec. Publ.*, 232, 63–73,
1222 <https://doi.org/10.1144/GSL.SP.2004.232.01.08>, 2004.
- 1223 de Boer, G. B. J., de Weerd, C., Thoenes, D., and Goossens, H. W. J.: Laser diffraction
1224 spectrometry: Fraunhofer diffraction versus Mie scattering, *Part. Charact.*, 4, 14–19, 1987.
- 1225 Boggs, S.: *Petrology of sedimentary rocks*, Cambridge University Press, New York, 600 pp.,
1226 2009.
- 1227 Bowman, E. T., Soga, K., and Drummond, W.: Particle shape characterisation using Fourier
1228 descriptor analysis, *Geotechnique*, 51, 545–554, <https://doi.org/10.1680/geot.2001.51.6.545>,
1229 2001.
- 1230 Bridges, N. T. and Muhs, D. R.: Duststones on mars: Source, transport, deposition, and
1231 erosion, *SEPM Spec. Publ.*, 102, 169–182, <https://doi.org/10.2110/pec.12.102.0169>, 2012.
- 1232 Van Den Bril, K. and Swennen, R.: Sedimentological control on carbonate cementation in the
1233 Luxembourg Sandstone Formation, *Geol. Belgica*, 12, 3–23, 2009.
- 1234 Brooks, H. L., Steel, E., and Moore, M.: Grain-Size Analysis of Ancient Deep-Marine
1235 Sediments Using Laser Diffraction, *Front. Earth Sci.*, 10, 1–24,
1236 <https://doi.org/10.3389/feart.2022.820866>, 2022.
- 1237 Bryon, D. N., Atherton, M. P., and Hunter, R. H.: The interpretation of granitic textures from
1238 serial thin sectioning, image analysis and three-dimensional reconstruction, *Mineral. Mag.*,
1239 59, 203–211, <https://doi.org/10.1180/minmag.1995.059.395.05>, 1995.



- 1240 Bull, W. B.: Relation of Textural (CM) Patterns to Depositional Environment of Alluvial-fan
1241 Deposits, *J. Sediment. Petrol.*, Vol. 32, 211–216, [https://doi.org/10.1306/74d70c7c-](https://doi.org/10.1306/74d70c7c-2b2111d7-8648000102c1865d)
1242 [2b2111d7-8648000102c1865d](https://doi.org/10.1306/74d70c7c-2b2111d7-8648000102c1865d), 1962.
- 1243 Buller, A. T. and McManus, J.: Modes of turbidites deposition deduced from grain-size
1244 analyses, *Geol. Mag.*, 109, 491–500, 1973.
- 1245 Burger, H. and Skala, W.: Comparison of sieve and thin-section technique by a MonteCarlo
1246 model, *Comput. Geosci.*, 2, 123–139, 1976.
- 1247 Bush, J.: Derivation of a Size-Frequency Curve from the Cumulative Curve, *J. Sediment.*
1248 *Petrol.*, Vol. 21, 178–182, <https://doi.org/10.1306/d4269463-2b26-11d78648000102c1865d>,
1249 1951.
- 1250 Cadigan, R. A.: Geologic interpretation of grain-size distribution measurements of Colorado
1251 Plateau sedimentary rocks, *J. Geol.*, 69, 121–143, 1961.
- 1252 Cavazza, W., Braga, R., Reinhardt, E. G., and Zanotti, C.: Influence of host-rock texture on
1253 the morphology of carbonate concretions in a meteoric diagenetic environment, *J. Sediment.*
1254 *Res.*, 79, 377–388, <https://doi.org/10.2110/jsr.2009.047>, 2009.
- 1255 Celia Magno, M., Venti, F., Bergamin, L., Gaglianone, G., Pierfranceschi, G., and Romano,
1256 E.: A comparison between Laser Granulometer and Sedigraph in grain size analysis of
1257 marine sediments, *Meas. J. Int. Meas. Confed.*, 128, 231–236,
1258 <https://doi.org/10.1016/j.measurement.2018.06.055>, 2018.
- 1259 Chayes, F.: A simple point counter for thin-section analysis, *Am. Mineral.*, 34, 1–11, 1949.
- 1260 Chayes, F.: On the bias of grain-size measurements made in thin section, *J. Geol.*, 58, 156–
1261 160, 1950.
- 1262 Cheetham, M. D., Keene, A. F., Bush, R. T., Sullivan, L. A., and Erskine, W. D.: A comparison
1263 of grain-size analysis methods for sand-dominated fluvial sediments, *Sedimentology*, 55,
1264 1905–1913, <https://doi.org/10.1111/j.1365-3091.2008.00972.x>, 2008.
- 1265 Coakley, J. P. and Syvitski, J. P. M.: SediGraph technique, in: Syvitski, J.M.P. (eds.)
1266 Principles, methods and application of particle size analysis., Cambridge University Press,
1267 Cambridge, UK., 129–142, 1991.
- 1268 Cooper, M. R. and Hunter, R. H.: Precision serial lapping, imaging and three-dimensional
1269 reconstruction of minus-cement and post-cementation intergranular pore-systems in the
1270 Penrith Sandstone of north-western England, *Mineral. Mag.*, 59, 213–220,
1271 <https://doi.org/10.1180/minmag.1995.059.395.06>, 1995.
- 1272 Cortinovis, S., Balsamo, F., and Storti, F.: Influence of analytical operating procedures on
1273 particle size distributions in carbonate cataclastic rocks, *J. Struct. Geol.*, 128, 103884,
1274 <https://doi.org/10.1016/j.jsg.2019.103884>, 2019.
- 1275 Cruz-Orive, L. M.: Distribution-free estimation of sphere size distributions from slabs showing
1276 overprojection and truncation, with a review of previous methods, *J. Microsc.*, 131, 265–290,
1277 1983.
- 1278 Dapples, E. C., Krumbein, W. C., and Sloss, L. L.: Petrographic and lithologic attributes of
1279 sandstones, *J. Geol.*, 61, 291–317, 1953.



- 1280 Davies, T. R. H., McSaveney, M. J., and Reznichenko, N. V.: What happens to fracture
1281 energy in brittle fracture? Revisiting the Griffith assumption, *Solid Earth*, 10, 1385–1395,
1282 <https://doi.org/10.5194/se-10-1385-2019>, 2019.
- 1283 Davis, S. N. and DeWiest, R. J. M.: *Hydrogeology*, Wiley & Sons, New York, 463 pp., 1966.
- 1284 Dimmen, V., Rotevatn, A., and Nixon, C. W.: The Relationship between Fluid Flow,
1285 Structures, and Depositional Architecture in Sedimentary Rocks: An Example-Based
1286 Overview, *Geofluids*, 1–19, <https://doi.org/10.1155/2020/3506743>, 2020.
- 1287 Doan, M.-L. and Gary, G.: Rock pulverization at high strain rate near the San Andreas fault,
1288 *Nat. Geosci.*, 2, 709–712, 2009.
- 1289 Dodd, R. T.: Accretion of the ordinary chondrites, *Earth Planet. Sci. Lett.*, 30, 281–291, 1976.
- 1290 Dutton, S. P., White, C. D., Willis, B. J., and Novakovic, D.: Calcite cement distribution and
1291 its effect on fluid flow in deltaic sandstone, *Frontier Formation, Wyoming*, *Am. Assoc. Pet.*
1292 *Geol. Bull.*, 86, 2007–2021, 2002.
- 1293 Easterbrook, D. J.: *Principles of Geomorphology*, McGraw-Hill, New York, 462 pp., 1969.
- 1294 Eicken, H.: Automated image analysis of ice thin sections: instrumentation, methods and
1295 extraction of stereological textural parameters, *J. Glaciol.*, 39, 341–352, 1993.
- 1296 Eisenhour, D. D.: Determining chondrule size distributions from thin-section
1297 measurements, *Meteorit. Planet. Sci.*, 31, 243–248,
1298 <https://doi.org/10.1111/j.19455100.1996.tb02019.x>, 1996.
- 1299 Elias, H.: *Stereology*, Springer-Verlag, New York, 335 pp., 1967.
- 1300 Engelder, J.-T.: Cataclasis and the generation of fault gouge, *Geol. Soc. Am. Bull.*, 85, 1515–
1301 1522, [https://doi.org/10.1130/0016-7606\(1974\)85<1515:catgof>2.0.co;2](https://doi.org/10.1130/0016-7606(1974)85<1515:catgof>2.0.co;2), 1974.
- 1302 Eychenne, J. and Engwell, S. L.: The grain size of volcanic fall deposits: Spatial trends and
1303 physical controls, *GSA Bull.*, 135, 1844–1858, <https://doi.org/10.1130/b36275.1>, 2022.
- 1304 Faure, G. and Mensing, T. M.: *Introduction to Planetary Science: The geological perspective*,
1305 Springer, Dordrecht, The Netherlands, 1–526 pp., <https://doi.org/10.1007/9781-4020-5544-7>,
1306 2007.
- 1307 Fernlund, J. M. R.: 3-D image analysis size and shape method applied to the evaluation of the
1308 Los Angeles test, *Eng. Geol.*, 77, 57–67, <https://doi.org/10.1016/j.enggeo.2004.08.002>, 2005.
- 1309 Fetter, C. W.: *Applied Hydrogeology*, 3rd ed., Prentice-Hall, Englewood Cliffs, New Jersey,
1310 USA, 691 pp., 1994.
- 1311 Folk, R. L.: A review of grain-size parameters, *Sedimentology*, 6, 73–93, 1966.
- 1312 Folk, R. L.: Petrology of sedimentary rocks, 170 pp.,
1313 <https://doi.org/10.1017/CBO9781107415324.004>, 1974.
- 1314 Folk, R. L. and Ward, W. C.: Brazos River bar: a study in the significance of grain size
1315 parameters, *J. Sediment. Petrol.*, 27, 3–26, 1957.
- 1316 Francus, P.: Using image analysis to estimate quantitatively some microstructural parameters
1317 of detrital sediments, *Geol. Belgica*, 2–3, 173–180, 1999.



- 1318 Fraser, H. J.: Experimental study of the porosity and permeability of clastic sediments, *J. Geol.*,
1319 43, 910–1010, 1935.
- 1320 Freeman, B. and Ferguson, C. C.: Deformation mechanism maps and micromechanics of
1321 rocks with distributed grain sizes, *J. Geophys. Res.*, 91, 3849–3860, 1986.
- 1322 Friedman, G. M.: Determination of sieve-size distribution from thin-section data for
1323 sedimentary petrological studies, *J. Geol.*, 66, 394–416, 1958.
- 1324 Friedman, G. M.: Comparison of Moment Measures for Sieving and Thin-Section Data in
1325 Sedimentary Petrological Studies, *SEPM J. Sediment. Res.*, Vol. 32, 15–25,
1326 <https://doi.org/10.1306/74d70c36-2b21-11d7-8648000102c1865d>, 1962a.
- 1327 Friedman, G. M.: On sorting, sorting coefficients, and the lognormality of the grain size
1328 distribution of sandstones, *J. Geol.*, 70, 737–753, 1962b.
- 1329 Friedman, G. M.: In defence of point counting analysis: hypothetical experiments versus real
1330 rocks, *Sedimentology*, 4, 247–253, 1965.
- 1331 Gallagher, C., Kerr, E., and McFadden, S.: Particle size distribution for additive
1332 manufacturing powder using stereological corrections, *Powder Technol.*, 429, 118873,
1333 <https://doi.org/10.1016/j.powtec.2023.118873>, 2023.
- 1334 Garzanti, E.: Petrographic classification of sand and sandstone, *Earth-Science Rev.*, 192,
1335 545–563, <https://doi.org/10.1016/j.earscirev.2018.12.014>, 2019.
- 1336 Giachetti, T., Trafton, K. R., Wiejaczka, J., Gardner, J. E., Watkins, J. M., Shea, T., and
1337 Wright, H. M. N.: The products of primary magma fragmentation finally revealed by pumice
1338 agglomerates, *Geology*, 49, 1307–1311, <https://doi.org/10.1130/G48902.1>, 2021.
- 1339 Goldbery, R. and Richardson, D.: The influence of bulk shape factors on settling velocities of
1340 natural sand-sized sedimentary suites, *Sedimentology*, 36, 125–136, 1989.
- 1341 Grassy, R. G.: Use of the Microprojector in the Mechanical Analysis of Small Samples of
1342 River Sand, *J. Sediment. Petrol.*, Vol. 13, 47–57, <https://doi.org/10.1306/d4269193-2b2611d7-8648000102c1865d>, 1943.
- 1344 Greenman, N. N.: The mechanical analysis of sediments from thin-section data, *J. Geol.*, 59,
1345 447–462, 1951.
- 1346 Griffiths, J. C.: Grain-size distribution and reservoir-rock characteristics, *Am. Assoc. Pet. Geol.*
1347 *Bull.*, 36, 205–229, <https://doi.org/10.1126/science.58.1489.27.b>, 1952.
- 1348 Griffiths, J. C.: Measurement of the properties of sediments, *J. Geol.*, 69, 487–497, 1961.
- 1349 Grotzinger, J. P. and Milliken, R. E.: The sedimentary rock record of mars: Distribution, origins,
1350 and global stratigraphy, 1–48 pp., <https://doi.org/10.2110/pec.12.102.0001>, 2012.
- 1351 Gualda, G. A. R.: Crystal size distributions derived from 3D datasets: Sample size versus
1352 uncertainties, *J. Petrol.*, 47, 1245–1254, <https://doi.org/10.1093/petrology/egl010>, 2006.
- 1353 Harrell, J. A. and Eriksson, K. A.: Empirical Conversion Equations for Thin-Section and Sieve
1354 Derived Size Distribution Parameters, *J. Sediment. Petrol.*, Vol. 49, 273–280,
1355 <https://doi.org/10.1306/212f7711-2b24-11d7-8648000102c1865d>, 1979.



- 1356 Heilbronner, R.: Automatic grain boundary detection and grain size analysis using
1357 polarization micrographs or orientation images, *J. Struct. Geol.*, 22, 969–981,
1358 [https://doi.org/10.1016/S0191-8141\(00\)00014-6](https://doi.org/10.1016/S0191-8141(00)00014-6), 2000.
- 1359 Heilbronner, R. and Barrett, S.: *Image Analysis in Earth Sciences - Microstructures and*
1360 *Textures of Earth Materials*, Springer, Heidelberg, 520 pp., 2014.
- 1361 Heilbronner, R. and Bruhn, D.: The influence of three-dimensional grain size distributions on
1362 the rheology of polyphase rocks, *J. Struct. Geol.*, 20, 695–705, 1998.
- 1363 Heilbronner, R. and Keulen, N.: Grain size and grain shape analysis of fault rocks,
1364 *Tectonophysics*, 427, 199–216, <https://doi.org/10.1016/j.tecto.2006.05.020>, 2006.
- 1365 Higgins, M. D.: Numerical modeling of crystal shapes in thin sections: Estimation of crystal
1366 habit and true size, *Am. Mineral.*, 79, 113–119, 1994.
- 1367 Higgins, M. D.: Measurement of crystal size distributions, *Am. Mineral.*, 85, 1105–1116,
1368 <https://doi.org/10.2138/am-2000-8-901>, 2000.
- 1369 Hirsch, D. M.: Controls on porphyroblast size along a regional metamorphic field gradient,
1370 *Contrib. to Mineral. Petrol.*, 155, 401–415, <https://doi.org/10.1007/s00410-007-0248-y>, 2008.
- 1371 Hughes, D. W.: A disaggregation and thin section analysis of the size and mass distribution
1372 of the chondrules in the Bjurböle and Chainpur meteorites, *Earth Planet. Sci. Lett.*, 38, 391–
1373 400, 1978a.
- 1374 Hughes, D. W.: Chondrule mass distribution and the Rosin and Weibull statistical functions,
1375 *Earth Planet. Sci. Lett.*, 39, 371–376, 1978b.
- 1376 Jébrak, M.: Hydrothermal breccias in vein-type ore deposits: A review of mechanisms,
1377 morphology and size distribution, *Ore Geol. Rev.*, 12, 111–134,
1378 [https://doi.org/10.1016/S0169-1368\(97\)00009-7](https://doi.org/10.1016/S0169-1368(97)00009-7), 1997.
- 1379 Jerram, D. A. and Higgins, M. D.: 3D analysis of rock textures: Quantifying igneous
1380 microstructures, *Elements*, 3, 239–245, <https://doi.org/10.2113/gselements.3.4.239>, 2007.
- 1381 Jerram, D. A., Mock, A., Davis, G. R., Field, M., and Brown, R. J.: 3D crystal size
1382 distributions: A case study on quantifying olivine populations in kimberlites, *Lithos*, 112, 223–
1383 235, <https://doi.org/10.1016/j.lithos.2009.05.042>, 2009.
- 1384 Johnson, M. R.: Thin section grain size analysis revisited, *Sedimentology*, 41, 985–999, 1994.
- 1385 Johnson, S. E., Song, W. J., Vel, S. S., Song, B. R., and Gerbi, C. C.: Energy Partitioning,
1386 Dynamic Fragmentation, and Off-Fault Damage in the Earthquake Source Volume, *J.*
1387 *Geophys. Res. Solid Earth*, 126, 1–38, <https://doi.org/10.1029/2021JB022616>, 2021.
- 1388 Kaminski, E. and Jaupart, C.: The size distribution of pyroclasts and the fragmentation
1389 sequence in explosive volcanic eruptions, *J. Geophys. Res. Solid Earth*, 103, 29759–29779,
1390 <https://doi.org/10.1029/98jb02795>, 1998.
- 1391 Keller, W. D.: Size distribution of sand in some dunes, beaches, and sandstones, *Am. Assoc.*
1392 *Pet. Geol. Bull.*, 29, 215–221, 1945.
- 1393 Kellerhals, R., Shaw, J., and Arora, V. K.: On grain size from thin sections, *J. Geol.*, 83, 79–
1394 96, 1975.



- 1395 Kennedy, S. K. and Mazzullo, J.: Image analysis method of grain size measurement, in:
1396 Syvitski, J.M.P. (eds.) Principles, methods and application of particle size analysis.,
1397 Cambridge University Press, Cambridge, UK., 76–87, 1991.
- 1398 Ketcham, R. A.: Computational methods for quantitative analysis of three-dimensional
1399 features in geological specimens, *Geosphere*, 1, 32–41,
1400 <https://doi.org/10.1130/GES00001.1>, 2005.
- 1401 Keulen, N., Heilbronner, R., Stünitz, H., Boullier, A. M., and Ito, H.: Grain size distributions of
1402 fault rocks: A comparison between experimentally and naturally deformed granitoids, *J.*
1403 *Struct. Geol.*, 29, 1282–1300, <https://doi.org/10.1016/j.jsg.2007.04.003>, 2007.
- 1404 Kimura, S., Ito, T., and Minagawa, H.: Grain-size analysis of fine and coarse non-plastic
1405 grains: comparison of different analysis methods, *Granul. Matter*, 20, 1–15,
1406 <https://doi.org/10.1007/s10035-018-0820-3>, 2018.
- 1407 Konert, M. and Vandenberghe, J.: Comparison of laser grain size analysis with pipette and
1408 sieve analysis: A solution for the underestimation of the clay fraction, *Sedimentology*, 44,
1409 523–535, <https://doi.org/10.1046/j.1365-3091.1997.d01-38.x>, 1997.
- 1410 Kong, M., Bhattacharya, R. N., James, C., and Basu, A.: A statistical approach to estimate
1411 the 3D size distribution of spheres from 2D size distributions, *Bull. Geol. Soc. Am.*, 117, 244–
1412 249, <https://doi.org/10.1130/B25000.1>, 2005.
- 1413 Kranck, K.: Grain-size characteristics of turbidites, *Geol. Soc. Spec. Publ.*, 15, 83–92,
1414 <https://doi.org/10.1144/GSL.SP.1984.015.01.05>, 1984.
- 1415 Krumbein, W. C.: The mechanical analysis of fine-grained sediments, *J. Sediment. Petrol.*, 2,
1416 140–149, 1932.
- 1417 Krumbein, W. C.: Thin-section mechanical analysis of indurated sediments, *J. Geol.*, 43, 482–
1418 496, 1935.
- 1419 Krumbein, W. C.: Size Frequency Distributions of Sediments and the Normal Phi Curve,
1420 *SEPM J. Sediment. Res.*, Vol. 8, 84–90, <https://doi.org/10.1306/d4269008-2b26-11d78648000102c1865d>, 1938.
- 1422 Krumbein, W. C.: Measurement and geological significance of shape and roundness of
1423 sedimentary particles, *J. Sediment. Petrol.*, 11, 64–72, 1941a.
- 1424 Krumbein, W. C.: The Effects of Abrasion on the Size, Shape and Roundness of Rock
1425 Fragments, *J. Geol.*, 49, 482–520, <https://doi.org/10.1086/624985>, 1941b.
- 1426 Krumbein, W. C. and Pettijohn, F. J.: *Manual of Sedimentary Petrography*, Appleton Century
1427 Crofts, New York, 549 pp., 1938.
- 1428 Krumbein, W. C. and Sloss, L.: *Stratigraphy and Sedimentation*, W.H. Freeman and Co, San
1429 Francisco, 660 pp., 1963.
- 1430 Kwan, A. K. H., Mora, C. F., and Chan, H. C.: Particle shape analysis of coarse aggregate
1431 using digital image processing, *Cem. Concr. Res.*, 29, 1403–1410,
1432 [https://doi.org/10.1016/S0008-8846\(99\)00105-2](https://doi.org/10.1016/S0008-8846(99)00105-2), 1999.



- 1433 Liu, Y., Liu, X., and Sun, Y.: QGrain: An open-source and easy-to-use software for the
1434 comprehensive analysis of grain size distributions, *Sediment. Geol.*, 423, 105980,
1435 <https://doi.org/10.1016/j.sedgeo.2021.105980>, 2021.
- 1436 Lopez-Sanchez, M. A.: Which average, how many grains, and how to estimate robust
1437 confidence intervals in unimodal grain size populations, *J. Struct. Geol.*, 135, 104042,
1438 <https://doi.org/10.1016/j.jsg.2020.104042>, 2020.
- 1439 Lopez-Sanchez, M. A. and Llana-Fúnez, S.: An extension of the Saltykov method to quantify
1440 3D grain size distributions in mylonites, *J. Struct. Geol.*, 93, 149–161,
1441 <https://doi.org/10.1016/j.jsg.2016.10.008>, 2016.
- 1442 Luther, A., Axen, G., and Selverstone, J.: Particle-size distributions of low-angle normal fault
1443 breccias: Implications for slip mechanisms on weak faults, *J. Struct. Geol.*, 55, 50–61,
1444 <https://doi.org/10.1016/j.jsg.2013.07.009>, 2013.
- 1445 Maithe, S. A., Brand, L. R., and Whitmore, J. H.: A methodology for disaggregation and
1446 textural analysis of quartz-cemented sandstones, *J. Sediment. Res.*, 89, 599–609,
1447 <https://doi.org/10.2110/jsr.2019.35>, 2019.
- 1448 Marone, C. and Scholz, C. H.: Particle size distribution and microstructures within simulated
1449 fault gouge, *J. Struct. Geol.*, 11, 799–814, 1989.
- 1450 Martin, P. M. and Mills, A. A.: Size and shape of near-spherical Allegan chondrules, *Earth
1451 Planet. Sci. Lett.*, 38, 385–390, 1978.
- 1452 Matthews, M. D.: The effect of grain shape and density on size measurement, in: Syvitski,
1453 J.M.P. (eds.) *Principles, methods and application of particle size analysis.*, Cambridge
1454 University Press, Cambridge, UK., 22–33, 1991a.
- 1455 Matthews, M. D.: The effect of pretreatment on size analysis, in: Syvitski, J.M.P. (eds.)
1456 *Principles, methods and application of particle size analysis.*, Cambridge University Press,
1457 Cambridge, UK., 34–42, 1991b.
- 1458 Mazzullo, J. and Kennedy, S. K.: Automated measurement of the nominal sectional diameters
1459 of individual sedimentary particles, *J. Sediment. Res.*, 55, 593–595, 1985.
- 1460 McBride, E. F., Milliken, K. L., Cavazza, W., Cibir, U., Fontana, D., Picard, M. D., and Zuffa,
1461 G. G.: Heterogeneous distribution of calcite cement at the outcrop scale in Tertiary
1462 sandstones, northern Apennines, Italy, *Am. Assoc. Pet. Geol. Bull.*, 79, 1044–1063,
1463 <https://doi.org/10.1306/8d2b21c3-171e-11d7-8645000102c1865d>, 1995.
- 1464 McCave, I. N. and Syvitski, J. M. P.: Principles and methods of geological particle size
1465 analysis, in: Syvitski, J.M.P. (eds.) *Principles, methods and application of particle size
1466 analysis.*, Cambridge University Press, Cambridge, UK., 3–21, 1991.
- 1467 McCave, I. N., Bryant, R. J., Cook, H. F., and Coughanowr, C. A.: Evaluation of a
1468 laser diffraction size analyzer for use with natural sediments, *J. Sediment. Res.*, 56, 561–564,
1469 1986.
- 1470 McPhie, J., Doyle, M., and Allen, R.: *Volcanic Tectures: a guide to the interpretation of textures
1471 in volcanic rocks*, University of Tasmania, Hobart, Australia, 196 pp., 1993.



- 1472 Means, W. D. and Park, Y.: New experimental approach to understanding igneous texture,
1473 *Geology*, 22, 323–326,
1474 [https://doi.org/10.1130/00917613\(1994\)022<0323:NEATUI>2.3.CO;2](https://doi.org/10.1130/00917613(1994)022<0323:NEATUI>2.3.CO;2), 1994.
- 1475 Menzies, J.: Micromorphological analyses of microfibrils and microstructures indicative of
1476 deformation processes in glacial sediments, in: Maltman, A.J., Hubbard, B. & Hambrey, M.J.
1477 (eds.) *Deformation of Glacial Materials*. Geological Society of London, Special Publications,
1478 176., 245–257, 2000.
- 1479 Middleton, G. V.: Hydraulic interpretation of sand size distributions, *J. Geodyn.*, 84, 405–426,
1480 1976.
- 1481 Milligan, T. G. and Kranck, K.: Electroresistance particle size analyzers, in: Syvitski, J.M.P.
1482 (eds.) *Principles, methods and application of particle size analysis.*, Cambridge University
1483 Press, 8, 109–118, 1991.
- 1484 Mock, A. and Jerram, D. A.: Crystal size distributions (CSD) in three dimensions: Insights
1485 from the 3D reconstruction of a highly porphyritic rhyolite, *J. Petrol.*, 46, 1525–1541,
1486 <https://doi.org/10.1093/petrology/egi024>, 2005.
- 1487 Molnia, B. L.: *Glacial Marine Sedimentation*, Plenum Press, New York, 844 pp., 1983.
- 1488 Montheil, L., Toy, V. G., Scott, J. M., Mitchell, T. M., and Dobson, D. P.: Impact of
1489 Coseismic Frictional Melting on Particle Size, Shape Distribution and Chemistry of
1490 Experimentally-Generated Pseudotachylite, *Front. Earth Sci.*, 8, 1–12,
1491 <https://doi.org/10.3389/feart.2020.596116>, 2020.
- 1492 Mora, C. F. and Kwan, A. K. H.: Sphericity, shape factor, and convexity measurement of
1493 coarse aggregate for concrete using digital image processing, *Cem. Concr. Res.*, 30, 351–
1494 358, [https://doi.org/10.1016/S0008-8846\(99\)00259-8](https://doi.org/10.1016/S0008-8846(99)00259-8), 2000.
- 1495 Morad, S., Ketzer, J. M., and DeRos, F.: Spatial and temporal distribution of diagenetic
1496 alterations in siliciclastic rocks: implication for mass transfer in sedimentary basins,
1497 *Sedimentology*, 47, 95–120, <https://doi.org/10.1046/j.1365-3091.2000.00007.x>, 2000.
- 1498 Morgan, D. J. and Jerram, D. A.: On estimating crystal shape for crystal size distribution
1499 analysis, *J. Volcanol. Geotherm. Res.*, 154, 1–7,
1500 <https://doi.org/10.1016/j.jvolgeores.2005.09.016>, 2006.
- 1501 Moss, A. J.: The physical nature of common sandy and pebbly deposits. Part 1, *Am. J. Sci.*,
1502 260, 337–373, 1962.
- 1503 Mozley, P. S. and Davis, J. M.: Relationship between oriented calcite concretions and
1504 permeability correlation structure in an alluvial aquifer, Sierra Ladrone Formation, New
1505 Mexico, *J. Sediment. Res.*, 66, 11–16, <https://doi.org/10.1306/D4268293-2B26-11D78648000102C1865D>, 1996.
- 1507 Mutti, E.: *Turbidite sandstones*, Agip, Istituto di Geologia, Università di Parma, San Donato
1508 Milanese, Milan, 256 pp., 1992.
- 1509 Nichols, G.: *Sedimentology and Stratigraphy*, Wiley, Chichester, UK, 419 pp.,
1510 <https://doi.org/10.1017/CBO9781107415324.004>, 2009.
- 1511 Packham, G. H.: Volume, weight and number-frequency analysis of sediments from
1512 thinsections data, *J. Geol.*, 63, 50–58, 1955.



- 1513 Panozzo Heilbronner, R.: Two-dimensional analysis of shape-fabric using projections of
1514 digitized lines in a plane, *Tectonophysics*, 95, 279–294, 1983.
- 1515 Panozzo Heilbronner, R.: The autocorrelation function: an image processing tool for fabric
1516 analysis, *Tectonophysics*, 212, 351–370, 1992.
- 1517 Panozzo, R.: Determination of size distribution of spheres from size distributions of circular
1518 section by Monte Carlo methods, *Microsc. Acta*, 86, 37–48, 1982.
- 1519 Passchier, C. W. and Trouw, R. A.: *Microtectonics*, 2nd ed., Springer, Berlin, 366 pp., 2005.
- 1520 De Pater, I. and Lissauer, J. J.: *Planetary Sciences*, Cambridge University Press, Cambridge,
1521 UK., 528 pp., 2001.
- 1522 Pettijohn, F. J., Potter, P. E., and Siever, R.: *Sand and sandstone*, Springer, New York, 618
1523 pp., 1972.
- 1524 Pickering, K. T. and Hiscott, R. N.: *Deep Marine Systems: Processes, Deposits, Environments,*
1525 *Tectonics and Sedimentation*, Wiley, 672 pp., 2015.
- 1526 Pizzati, M., Balsamo, F., Storti, F., Mozafari, M., Iacumin, P., Tinterri, R., and Swennen, R.:
1527 From axial parallel to orthogonal groundwater flow during fold amplification: insights from
1528 carbonate concretion development during the growth of the Quattro Castella Anticline,
1529 Northern Apennines, Italy, *J. Geol. Soc. London.*, 175, 806–819, 2018.
- 1530 Van Der Plas, L.: Preliminary note on the granulometric analysis of sedimentary rocks,
1531 *Sedimentology*, 1, 145–157, 1962.
- 1532 Powers, M. C.: A New Roundness Scale for Sedimentary Particles, *J. Sediment. Petrol.*, Vol.
1533 23, 117–119, <https://doi.org/10.1306/d4269567-2b26-11d7-8648000102c1865d>, 1953.
- 1534 Ranalli, G.: Grain size distribution and flow stress in tectonites, *J. Struct. Geol.*, 6, 443– 447,
1535 1984.
- 1536 Roberson, S. and Weltje, G. J.: Inter-instrument comparison of particle-size analysers,
1537 *Sedimentology*, 61, 1157–1174, <https://doi.org/10.1111/sed.12093>, 2014.
- 1538 Roethlisberger, H.: An adequate method of grain size determination in sections, *J. Geol.*, 63,
1539 579–584, 1955.
- 1540 Rose, H. E.: The determination of the grain-size distribution of a spherical granular material
1541 embedded in a matrix, *Sedimentology*, 10, 293–309, 1968.
- 1542 Rosenfeld, M. A., Jacobsen, L., and Ferm, J. C.: A comparison of sieve and thin-section
1543 technique for size analysis, *J. Geol.*, 61, 114–132, 1953.
- 1544 Russ, J. C.: *Practical Stereology*, Plenum Press, New York, 194 pp., 1986.
- 1545 Russ, J. C.: *Computer-assisted Microscopy: The Measurement and Analysis of Images*,
1546 Plenum Press, New York, 453 pp., 1990.
- 1547 Sahagian, D. L. and Proussevitch, A. A.: 3D particle size distributions from 2D observations:
1548 stereology for natural applications, *J. Volcanol. Geotherm. Res.*, 84, 173– 196,
1549 [https://doi.org/10.1016/S0377-0273\(98\)00043-2](https://doi.org/10.1016/S0377-0273(98)00043-2), 1998.



- 1550 Sahu, B. K.: Depositional Mechanisms from the Size Analysis of Clastic Sediments, *J.*
1551 *Sediment. Res.*, 34, 73–83, <https://doi.org/10.1306/74d70fce-2b21-11d78648000102c1865d>,
1552 1964.
- 1553 Sahu, B. K.: Thin section analysis of sandstones on weight-frequency basis, *Sedimentology*,
1554 7, 255–259, 1966.
- 1555 Sammis, C. G. and Ben-Zion, Y.: Mechanics of grain-size reduction in fault zones, *J.*
1556 *Geophys. Res. Solid Earth*, 113, 1–12, <https://doi.org/10.1029/2006JB004892>, 2008.
- 1557 Saxena, N., Day-Stirrat, R. J., Hows, A., and Hofmann, R.: Application of deep learning for
1558 semantic segmentation of sandstone thin sections, *Comput. Geosci.*, 152, 104778,
1559 <https://doi.org/10.1016/j.cageo.2021.104778>, 2021.
- 1560 Schäfer, A. and Teyssen, T.: Size, shape and orientation of grains in sands and sandstones:
1561 image analysis applied to rock thin sections, *Sediment. Geol.*, 52, 251–271, 1987.
- 1562 Schneider, C. A., Rasband, W. S., and Eliceiri, K. W.: NIH Image to ImageJ: 25 years of image
1563 analysis, *Nat. Methods*, 9, 671–675, 2012.
- 1564 Schulte, P., Lehmkuhl, F., Steininger, F., Loibl, D., Lockot, G., Protze, J., Fischer, P., and
1565 Stauch, G.: Influence of HCl pretreatment and organo-mineral complexes on laser diffraction
1566 measurement of loess-paleosol-sequences, *Catena*, 137, 392–405,
1567 <https://doi.org/10.1016/j.catena.2015.10.015>, 2016.
- 1568 Seelos, K. and Sirocko, F.: RADIUS - Rapid particle analysis of digital images by ultrahigh-
1569 resolution scanning of thin sections, *Sedimentology*, 52, 669–681,
1570 <https://doi.org/10.1111/j.1365-3091.2005.00715.x>, 2005.
- 1571 Selley, R. : Applied Sedimentology, 1–523 pp.,
1572 <https://doi.org/10.1017/CBO9781107415324.004>, 2001.
- 1573 Sibson, R. H.: Fault rocks and fault mechanisms, *J. Geol. Soc. London*, 133, 191–213, 1977.
- 1574 Singer, J. K., Anderson, J. B., Ledbetter, M. T., McCave, I. N., Jones, K. P. N., and Wright,
1575 R.: An assessment of analytical techniques for the size analysis of fine-grained sediments, *J.*
1576 *Sediment. Petrol.*, 58, 534–543, <https://doi.org/10.1306/212f8de6-2b24-11d78648000102c1865d>, 1988.
- 1578 Smith, R. E.: Grain size measurement in thin section and in grain mount, *J. Sediment. Res.*,
1579 36, 841–843, <https://doi.org/10.1306/74d71979-2b21-11d7-8648000102c1865d>, 1966.
- 1580 Song, B. R., Johnson, S. E., Song, W. J., Gerbi, C. C., and Yates, M. G.: Coseismic damage
1581 runs deep in continental strike-slip faults, *Earth Planet. Sci. Lett.*, 539, 116226,
1582 <https://doi.org/10.1016/j.epsl.2020.116226>, 2020.
- 1583 Spencer, D. W.: The interpretation of grain size distribution curves of clastic sediments, *J.*
1584 *Sediment. Petrol.*, 33, 180–190, 1952.
- 1585 Sperazza, M., Moore, J. N., and Hendrix, M. S.: High-resolution particle size analysis of
1586 naturally occurring very fine-grained sediment through laser diffractometry, *J. Sediment.*
1587 *Res.*, 74, 736–743, <https://doi.org/10.1306/031104740736>, 2004.
- 1588 Stauffer, P. H.: Thin section size analysis: a further note, *Sedimentology*, 7, 261–263, 1966.



- 1589 Stipp, M. and Tullis, J.: The recrystallized grain size piezometer for quartz, *Geophys. Res. Lett.*, 30, 1–5, <https://doi.org/10.1029/2003GL018444>, 2003.
1590
- 1591 Storti, F. and Balsamo, F.: Particle size distributions by laser diffraction: sensitivity of granular matter strength to analytical operating procedures, *Solid Earth*, 1, 25–48, <https://doi.org/10.5194/se-1-25-2010>, 2010.
1592
1593
- 1594 Storti, F., Billi, A., and Salvini, F.: Particle size distributions in natural carbonate fault rocks: Insights for non-self-similar cataclasis, *Earth Planet. Sci. Lett.*, 206, 173–186, [https://doi.org/10.1016/S0012-821X\(02\)01077-4](https://doi.org/10.1016/S0012-821X(02)01077-4), 2003.
1595
1596
- 1597 Syvitski, J. P. M., LeBlanc, K. W. G., and Asprey, K. W.: Interlaboratory, interinstrument calibration experiment, in: Syvitski, J.M.P. (eds.) *Principles, methods and application of particle size analysis.*, Cambridge University Press, Cambridge, UK., 174–193, 1991a.
1598
1599
- 1600 Syvitski, J. P. M., Asprey, K. W., and Clattenburg, D. A.: Principles, design, and calibration of settling tubes, in: Syvitski, J.M.P. (eds.) *Principles, methods and application of particle size analysis.*, Cambridge University Press, Cambridge, UK., 45–63, 1991b.
1601
1602
- 1603 Tafesse, S., Fernlund, J. M. R., and Bergholm, F.: Digital sieving-Matlab based 3-D image analysis, *Eng. Geol.*, 137–138, 74–84, <https://doi.org/10.1016/j.enggeo.2012.04.001>, 2012.
1604
- 1605 Taylor, M. A.: Quantitative measures for shape and size of particles, *Powder Technol.*, 124, 94–100, [https://doi.org/10.1016/S0032-5910\(01\)00476-4](https://doi.org/10.1016/S0032-5910(01)00476-4), 2002.
1606
- 1607 Théodon, L., Debayle, J., and Coufort-Saudejaud, C.: Morphological characterization of aggregates and agglomerates by image analysis: A systematic literature review, *Powder Technol.*, 430, 119033, <https://doi.org/10.1016/j.powtec.2023.119033>, 2023.
1608
1609
- 1610 Tiab, D. and Donaldson, E. C.: *Petrophysics*, 2nd ed., Elsevier, Burlington, USA, 889 pp., 2004.
1611
- 1612 Torabi, A. and Fossen, H.: Spatial variation of microstructure and petrophysical properties along deformation bands in reservoir sandstones, *Am. Assoc. Pet. Geol. Bull.*, 93, 919–938, <https://doi.org/10.1306/03270908161>, 2009.
1613
1614
- 1615 Udden, J. A.: Mechanical composition of clastic sediments, *Geol. Soc. Am. Bull.*, 25, 655–744, <https://doi.org/10.1130/gsab-25-655>, 1914.
1616
- 1617 Underwood, E. E.: *Quantitative Stereology*, 2nd ed., Addison-Wesley Publishing Company, Reading, MA, USA, 274 pp., 1970.
1618
- 1619 Wadell, H.: Sphericity and roundness of rock particles, *J. Geol.*, 41, 310–331, 1933.
1620
- 1621 Wadell, H.: Volume, shape and roundness of quartz particles, *J. Geol.*, 43, 250–280, 1935.
1622
- 1623 Washburn, A. L.: *Geocryology: A Survey of Periglacial Processes and Environment*, Edward Arnold Ltd., London, 406 pp., 1979.
1624
- 1623 Weiner, B. B.: Particle sizing using photon correlation spectroscopy, in: Barth, H.G. (eds.) *Modern methods of particle size analysis.*, Wiley, New York, 93–116, 1984.
1624
- 1625 Wentworth, C. K.: A Laboratory and Field Study of Cobble Abrasion, *J. Geol.*, 27, 507–521, <https://doi.org/10.1086/622676>, 1919.
1626

<https://doi.org/10.5194/egusphere-2023-2636>
Preprint. Discussion started: 15 November 2023
c Author(s) 2023. CC BY 4.0 License.



- 1627 Wentworth, C. K.: A Scale of Grade and Class Terms for Clastic Sediments, *J. Geol.*, 30, 377–
1628 392, <https://doi.org/10.1086/622910>, 1922.
- 1629 Wicksell, S. D.: The corpuscle problem, a mathematical study of a biometric problem,
1630 *Biometrika*, 17, 84–99, 1925.
- 1631 Zieg, M. J. and Marsh, B. D.: Crystal size distributions and scaling laws in the quantification
1632 of igneous textures, *J. Petrol.*, 43, 85–101, <https://doi.org/10.1093/petrology/43.1.85>, 2002.
1633